el (Le Belle *et al.*, 2011), and redox balance is important to regulate NSC/neural progenitor cell (NPC)-self-renewal and differentiation (Smith *et al.*, 2000; Li *et al.*, 2007; Hou *et al.*, 2012; Topchiy *et al.*, 2013). For example, mitochondrial superoxide negatively regulates NPC-self-renewal in the developmental cerebral cortex (Hou *et al.*, 2012). High levels of ROS inhibit O-2A progenitor proliferation (Smith *et al.*, 2000; Li *et al.*, 2007). In other cases, NADPH oxidase (Nox) 4-generated superoxide drives mouse NSC proliferation (Topchiy *et al.*, 2013). Ketamine-induced ROS enhanced the proliferation of NSCs derived from human embryonic stem cells (Bai *et al.*, 2013). The effect of ROS on NSC/NPC proliferation may change depending on the subcellular localization of the ROS generation and the timing of the ROS generation.

The suppression of NSC proliferation by the supernatants of both CNTs were virtually restored by the antioxidants, suggesting that the effects of CNT-supernatants were mediated through ROS stress. After a 5-hr sonication, multiple metals were detected in the SWCNT and MWCNT supernatants using ICP-MS. Mn, Rb, Cs, Tl, and Fe were detected in the SWCNT supernatant, and Mn, Cs, W, and Tl were detected in the MWCNT supernatant. Out of these SWCNT metals, the effects of Mn and Fe were reversed by antioxidants, suggesting that Mn and Fe play the main role in the suppression of NSC proliferation by CNT supernatants. In the MWCNT supernatant, the concentrations of Mn and Fe were insufficient to suppress NSC proliferation. Thus, a combination of ROS produced by multiple metals might produce synergistic suppressive effects.

Fe is essential for biological processes, but it is also known to be toxic in excess. Fe^{2+} overload into the cells and shuttling of Fe^{2+} to Fe^{3+} leads to cellular malfunctions due to ROS production (Halliwell and Gutteridge, 1992; Touati, 2000). Although Fe^{3+} has been largely considered as non-cytotoxic (Braun, 1997; Bruins *et al.*, 2000), it has its own mechanisms that can alter cell viability (Chamnongpol *et al.*, 2002). Fe^{3+} shows ROS production even while bound to proteins (Alekseenko *et al.*, 2008). GSH revealed pro-oxidant effects in the presence of an exogenous Fe^{3+} (Zager and Burkhart, 1998). Furthermore, Fe^{2+} and Fe^{3+} were shown to enter brain mitochondria and cause mitochondrial depolarization and ROS production (Sripetchwandee *et al.*, 2013). Mn is also essential for biological processes, but it has been known to be a neurotoxicant in excess. Mn induces oxidative stress (Choi *et al.*, 2007; Park and Park, 2010) and the release of cytokines (Park and Park, 2010). Mn further potentiates inflammation by the release of MMP9 through ROS production and modulation of ERK (Latronico *et al.*, 2013). Rb was also detected in the supernatants of SWCNT and MWCNT. Here, we found that Rb alone suppressed NSC proliferation in a ROS-independent manner. Rb has long been considered as nontoxic. Rb is generally used as a medical contrast medium because of its long half-life. Thus, the mechanism behind the Rb effects should be clarified quickly.

Most commercial CNTs contain ultrafine metal particles composed of Fe, Ni, Y, Co, Pb, and Cu that are used as catalysts (Ding *et al.*, 2008; Yazyev and Pasquarello, 2008; Banhart, 2009; Tyagi *et al.*, 2011). Recent studies showed that metal impurities play a major role in CNT cytotoxicity (Liu *et al.*, 2008; Kim *et al.*, 2010). The residual metals can remain in the contact solvent or embed inside the CNTs (Pumera, 2007; Fubini *et al.*, 2011; Aldieri *et al.*, 2013). In our study, the content of Fe in SWCNT was remarkable. A SWCNT is a graphene sheet protected metal core/shell of nanoparticles (Pumera, 2007). This structure may have caused the higher levels of metal impurities when compared with MWCNTs. Our data suggest that the residual metallic catalysts are released by vibration energy with a sonication frequency of 36 kHz, watt density of 65 W/264 cm^2 and sonication time of 5 hr. Pumera *et al.* indicated that washing with concentrated nitric acid removed up to 88% (w/w) of metal catalyst nanoparticles (Pumera, 2007). For public health and the safer applications of CNTs in nano-medicine, it is preferable to decrease the amount of the metal impurities by improving the washing process.

Conflict of interest---- The authors declare that there is no conflict of interest.

REFERENCES

Aldieri, E., Fenoglio, I., Cesano, F., Gazzano, E., Gulino, G., Scarano, D., Attanasio, A., Mazzucco, G., Ghigo, D. and Fubini, B. (2013): The role of iron impurities in the toxic effects exerted by short multiwalled carbon nanotubes (MWCNT) in murine alveolar macrophages. J. Toxicol. Environ. Health Part A, **76**, 1056-1071.

Alekseenko, A.V., Waseem, T.V. and Fedorovich, S.V. (2008): Ferritin, a protein containing iron nanoparticles, induces reactive oxygen species formation and inhibits glutamate uptake in rat brain synaptosomes. Brain Res., **1241**, 193-200.

Arfsten, D.P., Johnson, E.W., Wilfong, E.R., Jung, A.E. and Bobb, A.J. (2007): Distribution of radio-labeled N-Acetyl-L-Cysteine in Sprague-Dawley rats and its effect on glutathione metabolism following single and repeat dosing by oral gavage. Cutan. Ocul. Toxicol., **26**, 113-134.

Bai, X., Yan, Y., Canfield, S., Muravyeva, M.Y., Kikuchi, C., Zaja, I., Corbett, J.A. and Bosnjak, Z.J. (2013): Ketamine enhances human neural stem cell proliferation and induces neuronal apoptosis via reactive oxygen species-mediated mitochondrial pathway. Anesth. Analg., **116**, 869-880.

Balasubramanian, S.K., Poh, K.W., Ong, C.N., Kreyling, W.G., Ong, W.Y. and Yu, L.E. (2013): The effect of primary particle size on biodistribution of inhaled gold nano-agglomerates. Biomaterials, **34**, 5439-5452.

Banhart, F. (2009): Interactions between metals and carbon nanotubes: at the interface between old and new materials. Nanoscale, **1**, 201-213.

Belyanskaya, L., Weigel, S., Hirsch, C., Tobler, U., Krug, H.F. and Wick, P. (2009): Effects of carbon nanotubes on primary neurons and glial cells. Neurotoxicology, **30**, 702-711.

Braun, V. (1997): Avoidance of iron toxicity through regulation of bacterial iron transport. Biol. Chem., **378**, 779-786.

Bruins, M.R., Kapil, S. and Oehme, F.W. (2000): Microbial resistance to metals in the environment. Ecotoxicol. Environ. Saf., **45**, 198-207.

Carr, A. and Frei, B. (1999): Does vitamin C act as a pro-oxidant under physiological conditions? FASEB J., **13**, 1007-1024.

Caviness, V.S.Jr., Takahashi, T. and Nowakowski, R.S. (1995): Numbers, time and neocortical neuronogenesis: a general developmental and evolutionary model. Trends Neurosci., **18**, 379-383.

Chamnongpol, S., Dodson, W., Cromie, M.J., Harris, Z.L. and Groisman, E.A. (2002): Fe(III)-mediated cellular toxicity. Mol. Microbiol., **45**, 711-719.

Choi, C.J., Anantharam, V., Saetveit, N.J., Houk, R.S., Kanthasamy, A. and Kanthasamy, A.G. (2007): Normal cellular prion protein protects against manganese-induced oxidative stress and apoptotic cell death. Toxicol. Sci., **98**, 495-509.

Couillard-Despres, S., Iglseder, B. and Aigner, L. (2011): Neurogenesis, cellular plasticity and cognition: the impact of stem cells in the adult and aging brain--a mini-review. Gerontology, **57**, 559-564.

De la Fuente, M. and Victor, V.M. (2001): Ascorbic acid and N-acetylcysteine improve *in vitro* the function of lymphocytes from mice with endotoxin-induced oxidative stress. Free Radic. Res., **35**, 73-84.

Ding, F., Larsson, P., Larsson, J.A., Ahuja, R., Duan, H., Rosen, A. and Bolton, K. (2008): The importance of strong carbon-metal adhesion for catalytic nucleation of single-walled carbon nanotubes. Nano Lett., **8**, 463-468.

Donaldson, K., Poland, C.A., Murphy, F.A., MacFarlane, M., Chernova, T. and Schinwald, A. (2013): Pulmonary toxicity of carbon nanotubes and asbestos - similarities and differences. Adv. Drug Deliv. Rev., **65**, 2078-2086.

Eisch, A.J. and Petrik, D. (2012): Depression and hippocampal neurogenesis: a road to remission? Science, **338**, 72-75.

Ema, M., Matsuda, A., Kobayashi, N., Naya, M. and Nakanishi, J. (2011): Evaluation of dermal and eye irritation and skin sensitization due to carbon nanotubes. Regul.Toxicol. Pharmacol., **61**, 276-281.

Fubini, B., Fenoglio, I., Tomatis, M. and Turci, F. (2011): Effect of chemical composition and state of the surface on the toxic response to high aspect ratio nanomaterials. Nanomedicine (Lond), **6**, 899-920.

Gavello, D., Vandael, D.H., Cesa, R., Premoselli, F., Marcantoni, A., Cesano, F., Scarano, D., Fubini, B., Carbone, E., Fenoglio, I. and Carabelli, V. (2012): Altered excitability of cultured chromaffin cells following exposure to multi-walled carbon nanotubes. Nanotoxicology, **6**, 47-60.

Halliwell, B. and Gutteridge, J.M. (1992): Biologically relevant metal ion-dependent hydroxyl radical generation. An update. FEBS Lett., **307**, 108-112.

Hamanoue, M., Matsuzaki, Y., Sato, K., Okano, H.J., Shibata, S., Sato, I., Suzuki, S., Ogawara, M., Takamatsu, K. and Okano, H. (2009): Cell surface N-glycans mediated isolation of mouse neural stem cells. J. Neurochem., **110**, 1575-1584.

Henriksson, J. and Tjalve, H. (2000): Manganese taken up into the CNS via the olfactory pathway in rats affects astrocytes. Toxicol. Sci., **55**, 392-398.

Hou, Y., Ouyang, X., Wan, R., Cheng, H., Mattson, M.P. and Cheng, A. (2012): Mitochondrial superoxide production negatively regulates neural progenitor proliferation and cerebral cortical development. Stem Cells, **30**, 2535-2547.

Jaurand, M.C., Renier, A. and Daubriac, J. (2009): Mesothelioma: Do asbestos and carbon nanotubes pose the same health risk? Part. Fibre Toxicol., **6**, 16.

Kim, J.E., Lim, H.T., Minai-Tehrani, A., Kwon, J.T., Shin, J.Y., Woo, C.G., Choi, M., Baek, J., Jeong, D.H., Ha, Y.C., Chae, C.H., Song, K.S., Ahn, K.H., Lee, J.H., Sung, H.J., Yu, I.J., Beck, G.R.Jr. and Cho, M.H. (2010): Toxicity and clearance of intratracheally administered multiwalled carbon nanotubes from murine lung. J. Toxicol. Environ. Health Part A, **73**, 1530-1543.

Kim, K.K., Singh, R.K., Strongin, R.M., Moore, R.G., Brard, L. and Lange, T.S. (2011): Organometallic iron(III)-salophene exerts cytotoxic properties in neuroblastoma cells via MAPK activation and ROS generation. PloS One, **6**, e19049.

Kojo, S. (2004): Vitamin C: basic metabolism and its function as an index of oxidative stress. Curr. Med. Chem., **11**, 1041-1064.

Kriegstein, A. and Alvarez-Buylla, A. (2009): The glial nature of embryonic and adult neural stem cells. Ann. Rev. Neurosci., **32**, 149-184.

Latronico, T., Brana, M.T., Merra, E., Fasano, A., Di Bari, G., Casalino, E. and Liuzzi, G.M. (2013): Impact of manganese neurotoxicity on MMP-9 production and superoxide dismutase activity in rat primary astrocytes. Effect of resveratrol and therapeutical implications for the treatment of CNS diseases. Toxicol. Sci., **135**, 218-228.

Le Belle, J.E., Orozco, N.M., Paucar, A.A., Saxe, J.P., Mottahedeh, J., Pyle, A.D., Wu, H. and Kornblum, H.I. (2011): Proliferative neural stem cells have high endogenous ROS levels that regulate self-renewal and neurogenesis in a PI3K/Akt-dependant manner. Cell Stem Cell, **8**, 59-71.

Li, W., Nie, S., Yu, Q. and Xie, M. (2009): (-)-Epigallocatechin-3-gallate induces apoptosis of human hepatoma cells by mitochondrial pathways related to reactive oxygen species. J. Agric. Food Chem., **57**, 6685-6691.

Li, Z., Dong, T., Proschel, C. and Noble, M. (2007): Chemically diverse toxicants converge on Fyn and c-Cbl to disrupt precursor cell function. PLoS Biol., **5**, e35.

Liu, X., Guo, L., Morris, D., Kane, A.B. and Hurt, R.H. (2008): Targeted Removal of Bioavailable Metal as a Detoxification Strategy for Carbon Nanotubes. Carbon, **46**, 489-500.

Matsumoto, M., Serizawa, H., Sunaga, M., Kato, H., Takahashi, M., Hirata-Koizumi, M., Ono, A., Kamata, E. and Hirose, A. (2012): No toxicological effects on acute and repeated oral gavage doses of single-wall or multi-wall carbon nanotube in rats. J. Toxicol. Sci., **37**, 463-474.

Mistry, A., Stolnik, S. and Illum, L. (2009): Nanoparticles for direct nose-to-brain delivery of drugs. Int. J. Pharm., **379**, 146-157.

Nakajima, Y., Tsuruma, K., Shimazawa, M., Mishima, S. and Hara, H. (2009): Comparison of bee products based on assays of antioxidant capacities. BMC Complement. Altern. Med., **9**, 4.

Pacurari, M., Castranova, V. and Vallyathan, V. (2010): Single- and multi-wall carbon nanotubes versus asbestos: are the carbon nanotubes a new health risk to humans? J. Toxicol. Environ. Health A., **73**, 378-395.

Park, E.J. and Park, K. (2010): Induction of oxidative stress and inflammatory cytokines by manganese chloride in cultured T98G cells, human brain glioblastoma cell line. Toxicol. In Vitro, **24**, 472-479.

Persson, E., Henriksson, J. and Tjalve, H. (2003): Uptake of cobalt from the nasal mucosa into the brain via olfactory pathways in rats. Toxicol. Lett., **145**, 19-27.

Pumera, M. (2007): Carbon nanotubes contain residual metal catalyst nanoparticles even after washing with nitric acid at elevated temperature because these metal nanoparticles are sheathed by several graphene sheets. Langmuir, **23**, 6453-6458.

Reynolds, B.A., Tetzlaff, W. and Weiss, S. (1992): A multipotent EGF-responsive striatal embryonic progenitor cell produces neurons and astrocytes. J. Neurosci., **12**, 4565-4574.

Rolando, C. and Taylor, V. (2014): Neural stem cell of the hippocampus: development, physiology regulation, and dysfunction in disease. Curr Top Dev Biol., **107**, 183-206.

Roth, J.A. and Eichhorn, M. (2013): Down-regulation of LRRK2 in control and DAT transfected HEK cells increases manganese-induced oxidative stress and cell toxicity. Neurotoxicology, **37**, 100-107.

Sharma, H.S. and Sharma, A. (2007): Nanoparticles aggravate heat stress induced cognitive deficits, blood-brain barrier disruption, edema formation and brain pathology. Prog. Brain Res., **162**, 245-273.

Smith, J., Ladi, E., Mayer-Proschel, M. and Noble, M. (2000): Redox state is a central modulator of the balance between self-renewal and differentiation in a dividing glial precursor cell. Proceedings of the National Academy of Sciences of the United States of America, **97**, 10032-10037.

Sripetchwandee, J., Sanit, J., Chattipakorn, N. and Chattipakorn, S.C. (2013): Mitochondrial calcium uniporter blocker effectively prevents brain mitochondrial dysfunction caused by iron overload. Life Sci., **92**, 298-304.

Topchiy, E., Panzhinskiy, E., Griffin, W.S., Barger, S.W., Das, M. and Zawada, W.M. (2013): Nox4-generated superoxide drives angiotensin II-induced neural stem cell proliferation. Dev. Neurosci., **35**, 293-305.

Touati, D. (2000): Iron and oxidative stress in bacteria. Arch. Biochem. Biophys., **373**, 1-6.

Tyagi, P.K., Janowska, I., Cretu, O., Pham-Huu, C. and Banhart, F. (2011): Catalytic action of gold and copper crystals in the growth of carbon nanotubes. J. Nanosci. Nanotechnol., **11**, 3609-3615.

Xu, L.J., Zhao, J.X., Zhang, T., Ren, G.G. and Yang, Z. (2009): *In vitro* study on influence of nano particles of CuO on CA1 pyramidal neurons of rat hippocampus potassium currents. Environ. Toxicol., **24**, 211-217.

Yazyev, O.V. and Pasquarello, A. (2008): Effect of metal elements in catalytic growth of carbon nanotubes. Phys. Rev. Lett., **100**, *156102*.

Yim, M.B., Chae, H.Z., Rhee, S.G., Chock, P.B. and Stadtman, E.R. (1994): On the protective mechanism of the thiol-specific antioxidant enzyme against the oxidative damage of biomacromolecules. J. Biol. Chem., **269**, 1621-1626.

Zager, R.A. and Burkhart, K.M. (1998): Differential effects of glutathione and cysteine on Fe2+, Fe3+, H2O2 and myoglobin-induced proximal tubular cell attack. Kidney Int., **53**, 1661-1672.

Zhang, Z., Teruya, K., Eto, H. and Shirahata, S. (2011): Fucoidan extract induces apoptosis in MCF-7 cells via a mechanism involving the ROS-dependent JNK activation and mitochondria-mediated pathways. PloS One, **6**, e27441.

SCIENTIFIC REPORTS

OPEN

SUBJECT AREAS:
METABOLOMICS
ENVIRONMENTAL SCIENCES

Received
17 February 2014

Accepted
15 July 2014

Published
5 August 2014

Correspondence and requests for materials should be addressed to Y.Ka (kanda@nihs.go.jp)

NAD-dependent isocitrate dehydrogenase as a novel target of tributyltin in human embryonic carcinoma cells

Shigeru Yamada[1], Yaichiro Kotake[2], Yosuke Demizu[3], Masaaki Kurihara[3], Yuko Sekino[1] & Yasunari Kanda[1]

[1]Division of Pharmacology, National Institute of Health Sciences, Tokyo, Japan, [2]Graduate School of Biomedical and Health Sciences, Hiroshima University, Hiroshima, Japan, [3]Division of Organic Chemistry, National Institute of Health Sciences, Tokyo, Japan.

Tributyltin (TBT) is known to cause developmental defects as endocrine disruptive chemicals (EDCs). At nanomoler concentrations, TBT actions were mediated by genomic pathways via PPAR/RXR. However, non-genomic target of TBT has not been elucidated. To investigate non-genomic TBT targets, we performed comprehensive metabolomic analyses using human embryonic carcinoma NT2/D1 cells. We found that 100 nM TBT reduced the amounts of α-ketoglutarate, succinate and malate. We further found that TBT decreased the activity of NAD-dependent isocitrate dehydrogenase (NAD-IDH), which catalyzes the conversion of isocitrate to α-ketoglutarate in the TCA cycle. In addition, TBT inhibited cell growth and enhanced neuronal differentiation through NAD-IDH inhibition. Furthermore, studies using bacterially expressed human NAD-IDH and in silico simulations suggest that TBT inhibits NAD-IDH due to a possible interaction. These results suggest that NAD-IDH is a novel non-genomic target of TBT at nanomolar levels. Thus, a metabolomic approach may provide new insights into the mechanism of EDC action.

Endocrine disruptive compounds (EDCs) have been studied extensively in environmental biology[1]. A large number of EDCs are known to cause genomic action via nuclear receptor. For example, xenoestrogens such as bisphenol A, genistein and diethylstilbestrol can bind to the estrogen receptor (ER) in the cell nucleus, followed by the alteration of gene expression[2,3]. In addition, EDCs induce the activation of non-genomic signaling pathways. For example, xenoestrogens increase intracellular calcium levels, activating eNOS and signaling cascades such as PI3K/AKT and MAPK[4–7]. Thus, both genomic and non-genomic pathways are required to understand the mechanism of EDC action.

Organotin compounds, such as tributyltin (TBT) are typical environmental contaminants and well known to cause developmental defects as EDCs. For example, TBT can cause increased fetal mortality, decreased fetal birth weights, and behavioral abnormalities in rat offspring[8,9]. Although the use of TBT has already been restricted, butyltin compounds, including TBT, can still be found in human blood at concentrations between 50 and 400 nM[10]. Several studies revealed that TBT activates retinoid X receptor (RXR) and/or peroxisome proliferator-activated receptor γ (PPARγ). These genomic transcriptional activations result in developmental effects, such as the imposex in many marine species[11–13] and the enhancement of adipocyte differentiation in mammals[14,15]. These TBT actions involve a higher binding affinity compared to intrinsic ligands at nM concentrations. In addition to the genomic effects, non-genomic action of TBT has been also reported. For example, TBT has been reported to inhibit the steroid biosynthesis pathway, which is responsible for the production of estrogen and androgen[16–18]. Another report has shown that TBT inhibits mitochondrial F1F0 ATP synthase[19]. These data were obtained at μM concentrations. Thus, the mechanism of nM concentrations of TBT has not been elucidated at a non-genomic level. In a previous study, we reported that treatment with 100 nM TBT resulted in growth arrest by targeting the glycolytic systems of the human embryonic carcinoma cell line NT2/D1[20]. Therefore, we raised the possibility that nM concentrations of TBT may target other non-genomic pathways which are involved in energy metabolism.

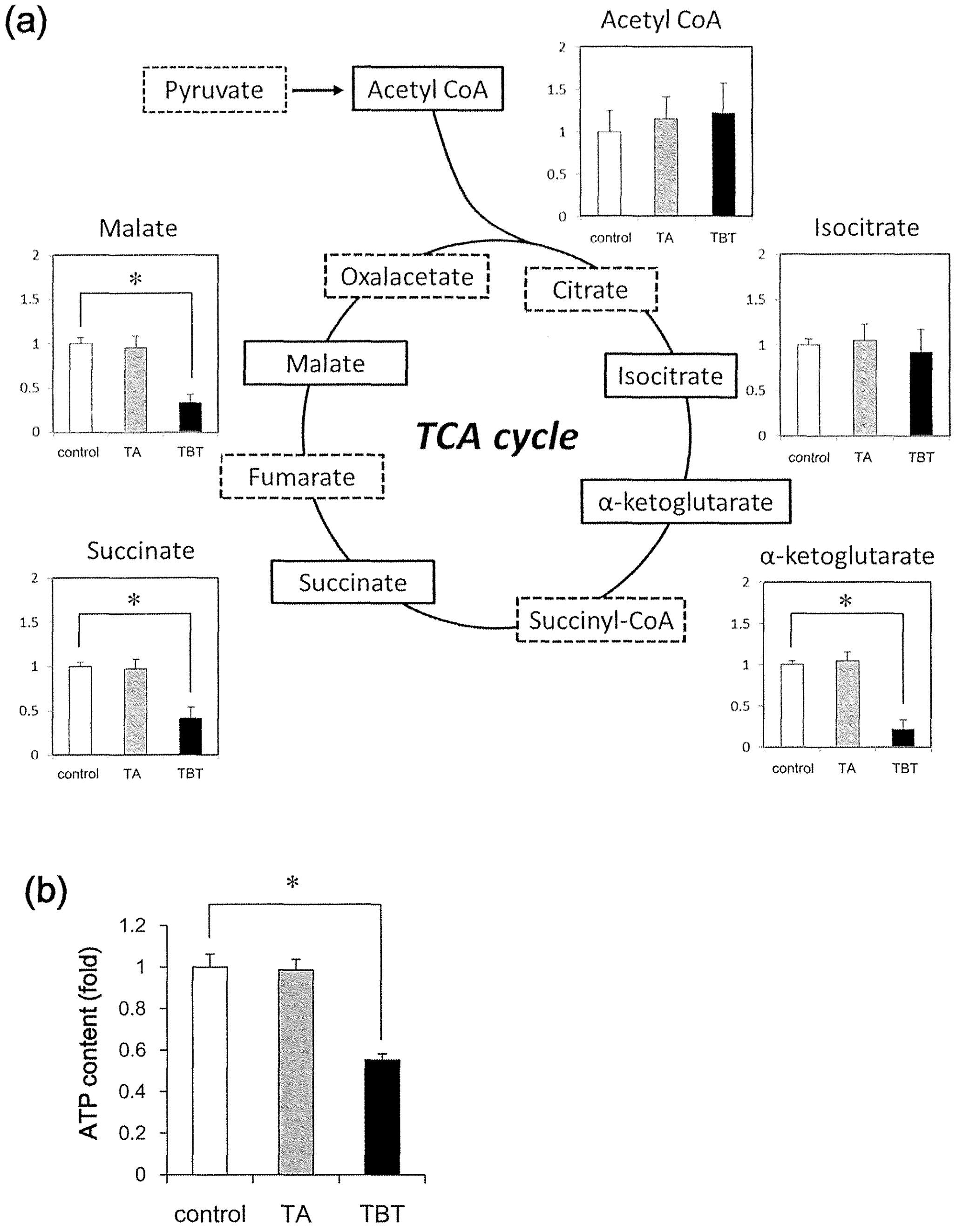

Figure 1 | Metabolomic analysis of NT2/D1 cells exposed to TBT. The cells were exposed to 100 nM TBT or TA for 24 h. (a) The levels of several metabolites, such as acetyl CoA, isocitrate, α-ketoglutarate, succinate and malate, were determined using CE-TOFMS. (b) The intracellular ATP content was determined in the lysed cells. * $P < 0.05$ compared with the corresponding control group.

In the present study, we investigated the molecular target of TBT at nM levels by comprehensive determination of the intracellular metabolites in NT2/D1 cells after TBT exposure. We found that exposure to 100 nM TBT reduced ATP production via NAD-dependent isocitrate dehydrogenase (NAD-IDH) in the cells. This NAD-IDH inhibition resulted in the reduction of the TCA cycle metabolites. In addition, TBT caused neural differentiation through an NAD-IDH-dependent mechanism. We report here that our metabolomic analysis revealed that NAD-IDH is a novel target of TBT in embryonic carcinoma cells.

Results

Metabolomic analysis of NT2/D1 cells exposed to TBT at nM levels. To investigate the non-genomic effects of a well-known endocrine disruptor TBT in human NT2/D1 embryonic carcinoma cells, we comprehensively determined intracellular metabolites using LC/MS. We found that exposure to 100 nM TBT reduced the amounts of TCA cycle components, such as α-ketoglutarate, succinate and malate (Figure 1a). The amounts of acetyl CoA and isocitrate were not changed. We also found that treatment with 100 nM TBT reduced the ATP content of the cells (Figure 1b). In contrast to TBT, exposure to the less toxic tin acetate (TA) did not affect the amount of each metabolite. These data suggest that TBT exposure decreases the amounts of TCA cycle metabolites, resulting in a reduction of ATP content.

NAD-IDH enzyme activity of NT2/D1 cells exposed to TBT at nM levels. Based on the results of the metabolomic analysis, we focused

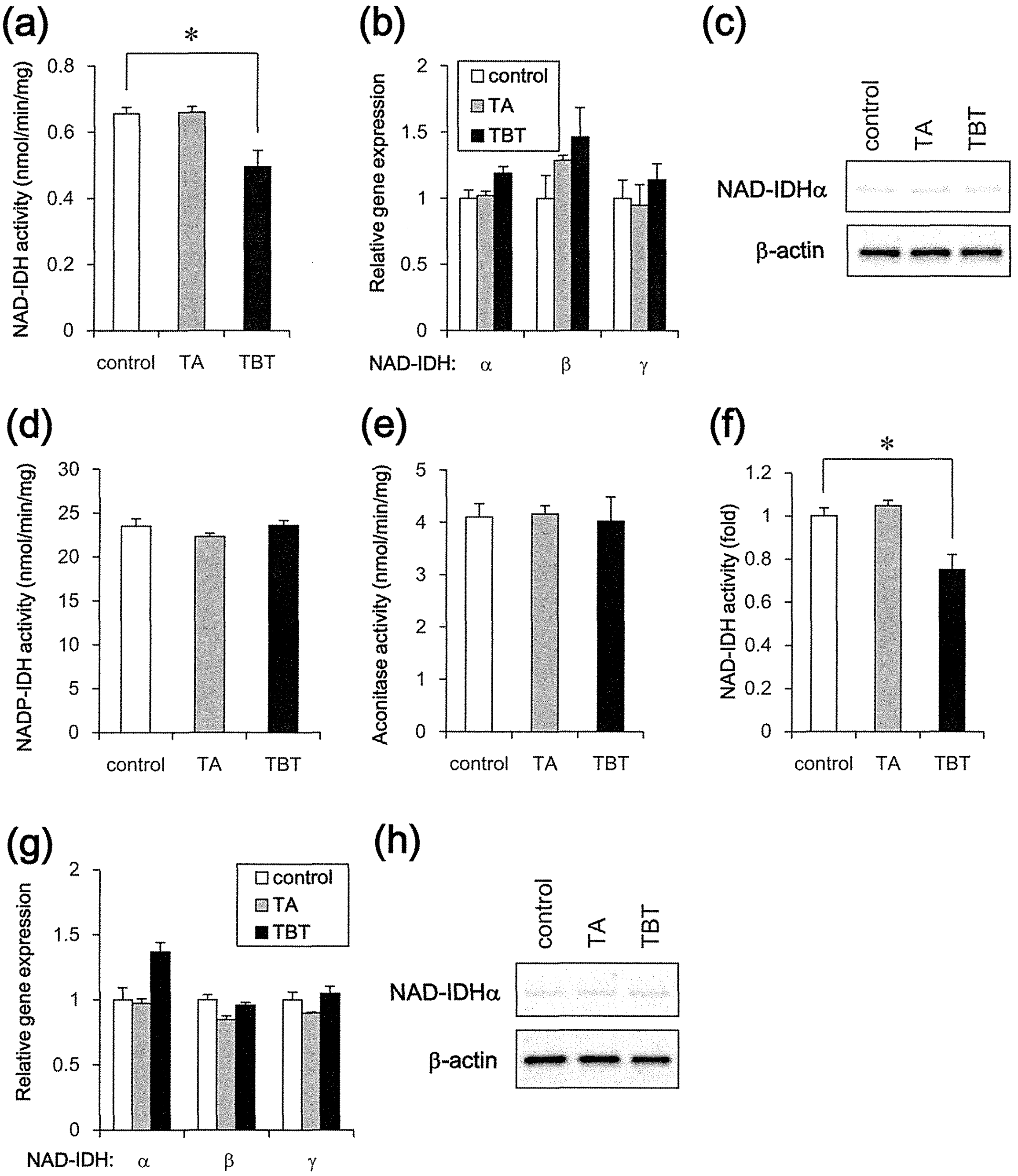

Figure 2 | Effect of TBT exposure on NAD-IDH enzyme activity in NT2/D1 cells. The cells were exposed to 100 nM TBT or TA for 24 h. (a) NAD-IDH activity was determined in the lysed cells. (b) The relative expressions of NAD-IDHα, β, and γ were measured using real-time PCR. The relative changes were normalized to the levels of RPL13. (c) The expression of NAD-IDHα protein was examined by western blot analysis using the anti-NAD-IDHα and anti-β-actin antibodies. Cropped blots were shown and the full-length blots were indicated in Supplementary Fig. 4. (d) NADP-IDH activity was determined in the lysed cells. (e) Aconitase activity was determined in the lysed cells. (f) To induce neuronal differentiation, the NT2/D1 cells were treated with 10 μM retinoic acid (RA) for 14 days. After exposure to 100 nM TBT for 24 h, NAD-IDH activity was determined in the lysed cells. (g) The relative expression levels of NAD-IDHα, β, and γ in the differentiated cells were measured using real-time PCR. The relative changes were normalized to the levels of RPL13. (h) The expression of NAD-IDHα protein was examined by western blot analysis using the anti-NAD-IDHα and anti-β-actin antibodies. Cropped blots were shown and the full-length blots were indicated in Supplementary Fig. 4. * $P < 0.05$ compared with the corresponding control group.

on isocitrate dehydrogenase, which catalyzes the conversion of isocitrate to α-ketoglutarate in the TCA cycle. Eukaryotes have different types of isocitrate dehydrogenases, such as NAD-dependent form (NAD-IDH; EC 1.1.1.41) and NADP-dependent form (NADP-IDH; EC 1.1.1.42)[21]. NAD-IDH is first rate-limiting enzyme in the TCA cycle and catalyzes an irreversible reaction, while NADP-IDH is involved in reversible reaction for biosynthesis via production of NADPH. As shown in Figure 2a, NAD-IDH activity was significantly reduced following TBT treatment. Since NAD-IDH is a heterotetramer composed of two α subunits (catalytic subunit), one β subunit and one γ subunit (regulatory subunit), we examined the expression of each subunit gene. Real-time PCR analysis showed that the expression of the NAD-IDHα, β and γ genes was not significantly changed by TBT exposure (Figure 2b). The protein expression of catalytic α subunits was not also changed by TBT exposure (Figure 2c). TA exposure did not affect either the enzyme activity or the NAD-IDH expression. We next examined the effect of TBT on NADP-IDH. The activity of NADP-IDH was not affected by TBT exposure (Figure 2d). We further examined the activity of aconitase (EC 4.2.1.3.), which catalyzes the conversion of citrate to isocitrate in the TCA cycle. Aconitase activity was also not affected by TBT exposure (Figure 2e). Thus, these data suggest that the inhibitory effect of TBT is specific to NAD-IDH in the TCA cycle.

To investigate whether TBT cytotoxicity was caused by a genomic transcriptional regulation, we tested the effects of the protein synthesis inhibitor cycloheximide in NT2/D1 cells. Treatment with cycloheximide did not alter the inhibitory effects of TBT on NAD-IDH activity (Figure S1a) and intracellular ATP production (Figure S2a). Moreover, the PPARγ agonist rosiglitazone did not reduce NAD-IDH activity (Figure S1b) and ATP content (Figure S2b). These results suggest that transcriptional regulation is not involved in the inhibition of NAD-IDH activity by TBT.

To examine whether the effect of TBT was selective for embryonic cells, we used NT2/D1 cells that had differentiated in response to retinoic acid. We observed that TBT also inhibited NAD-IDH activity in the differentiated NT2/D1 cells (Figure 2f). Real-time PCR analysis showed that the expression of the NAD-IDHα, β, and γ genes was not significantly affected by TBT exposure (Figure 2g). The protein expression of catalytic α subunits was not also changed by TBT exposure (Figure 2h). TA exposure did not affect either the activity or the NAD-IDH expression. These data suggest that TBT reduces NAD-IDH enzyme activity regardless of the developmental stage of the embryonic carcinoma cells.

Neuronal differentiation of RA-treated NT2/D1 cells exposed to TBT at nM levels. It has been reported that ATP content decreases during the differentiation of human embryonic stem cells into neural stem cells (NSCs)[22]. Therefore, the reduction of ATP caused by TBT treatment might be involved in neuronal differentiation. Moreover, TBT has been reported to cause cell growth arrest in NT2/D1 cells[20]. Because cell growth is generally reduced during differentiation, we examined whether TBT affects the neuronal differentiation process in NT2/D1 cells. Real-time PCR analysis revealed that retinoic acid (RA)-treated NT2/D1 cells showed increased expression of the differentiation markers NeuroD and Math1, confirming that neural differentiation had occurred (Figure 3a). Furthermore, we observed that TBT exposure enhanced the expression levels of these neuronal differentiation markers. Treatment with rosiglitazone had little effect on their expression (Figure S3), suggesting that PPARγ is not involved in neuronal differentiation. Taken together, these data suggest that TBT promotes neuronal differentiation.

Effect of NAD-IDH knockdown on neuronal differentiation in RA-treated NT2/D1 cells. To further investigate whether the neuronal differentiation triggered by TBT exposure is through an NAD-IDH-dependent mechanism, we performed knockdown (KD) of NAD-IDHα, the catalytic subunit of NAD-IDH, using lentivirus-delivered shRNAs. Real-time PCR analysis showed that KD efficiency was approximately 40% (Figure 3b). Due to the partial KD of the NAD-IDHα gene, NAD-IDH activity decreased to a level (22%) comparable to its level following TBT inhibition (24%) (Figure 3c). Further reduction of NAD-IDH activity was not significantly observed after TBT exposure in the NAD-IDHα KD cells. Similar to the effect of TBT, NAD-IDHα KD also reduced the ATP content of the cells (Figure 3d), and caused cell growth inhibition (Figure 3e). Further inhibition of ATP content and cell growth was not significantly observed after TBT exposure in the NAD-IDHα KD cells, suggesting that the NAD-IDH is a possible target of TBT. In addition, we found that NAD-IDHα KD significantly upregulated the expression of the neuronal differentiation markers NeuroD and Math1 (Figure 3f). These data suggest that NAD-IDH mediates TBT-induced neuronal differentiation in embryonic NT2/D1 cells.

NAD-IDH enzyme activity in the brain of rats orally exposed to TBT at low doses. To examine whether the in vitro inhibitory effect of TBT on NAD-IDH is also observed in vivo, adult rats were orally exposed to TBT at doses of 5 and 50 mg/kg. NAD-IDH activity in the cerebral cortex was significantly reduced following exposure to both doses of TBT (Figure 4a). Real-time PCR analysis showed that the expression of the NAD-IDHα, β, and γ genes was not significantly affected by TBT (Figure 4b). The protein expression of catalytic α subunits was not also affected by TBT (Figure 4c). NADP-IDH and aconitase activities were not affected by exposure to either dose of TBT (Figure 4d and e). These data suggest that TBT inhibits NAD-IDH activity both in vitro and in vivo.

Reduction of recombinant hNAD-IDH enzyme activity in E. coli lysate treated with TBT at nM levels. To investigate the mechanism by which TBT inhibits NAD-IDH activity, we examined whether TBT possibly interacts with NAD-IDH or not. Since NAD-IDHα subunit alone has been reported to show no detectable IDH activity, we used an Escherichia coli co-expression system of recombinant human (h) NAD-IDHα,β,γ subunits[23]. As shown in Figure 5a, we confirmed the expression of α subunit of hNAD-IDH protein in the extracts of E. coli transformants using western blot analysis. To check the activity of the recombinant hNAD-IDH, we used irreversible and allosteric NAD-IDH regulators. ADP has been reported to activate NAD-IDH allosterically by lowering the Km for the substrate isocitrate[24]. As expected, ADP increased the activity of hNAD-IDH in our assay system. Conversely, Zn^{2+} has been reported to inhibit several metabolic enzymes, including NAD-IDH, in hepatocytes[25]. We confirmed that Zn^{2+} reduces hNAD-IDH activity. Then, we examined whether TBT directly inhibits hNAD-IDH activity by adding TBT to the E. coli extracts containing hNAD-IDH. Treatment with 100 nM TBT for 1 h significantly reduced the hNAD-IDH activity (Figure 5b). Treatment with TA had little effect. Taken together, these data suggest that TBT inhibits hNAD-IDH activity through its possible interaction, but again we can not be sure that it is through direct binding with the data we have.

***In silico* docking simulation analysis.** To further consider this possible interaction between TBT and hNAD-IDH, we estimate TBT accessibility into hNAD-IDH (EC 1.1.1.41) α and hNADP-IDH (EC 1.1.1.42) homodimers by homology modeling and docking studies. We show the overlaid structure of the calculated hNAD-IDHα and hNADP-IDH (Figure 6a). The ligand binding pocket of hNAD-IDHα was larger than that of hNADP-IDH (Figure 6b). In our docking simulation, TBT was able to access the hNAD-IDHα ligand-binding pocket, whereas the hNADP-IDH pocket was not spacious enough to accommodate TBT (Figure 6c and d). Thus, these studies suggest that the selective inhibition of NAD-IDH by TBT may be due to differences in the pocket volumes between hNAD-IDHα and hNADP-IDH.

Discussion

In the present study, we demonstrate that NAD-IDH is a novel non-genomic target of TBT at nM levels both in vitro and in vivo. We showed that exposure to nM concentrations of TBT reduced the activity of NAD-IDH due to its possible interaction. We also found that TBT exposure caused both inhibition of cell growth and enhancement of neuronal differentiation through its inhibitory effect of NAD-IDH.

Our data suggest that NAD-IDH is a novel target molecule of TBT action. NAD-IDH is a NAD-dependent form of IDH found in NT2/D1 cells and the rat brain (Figure 2–4). Because NAD-IDH is ubi-

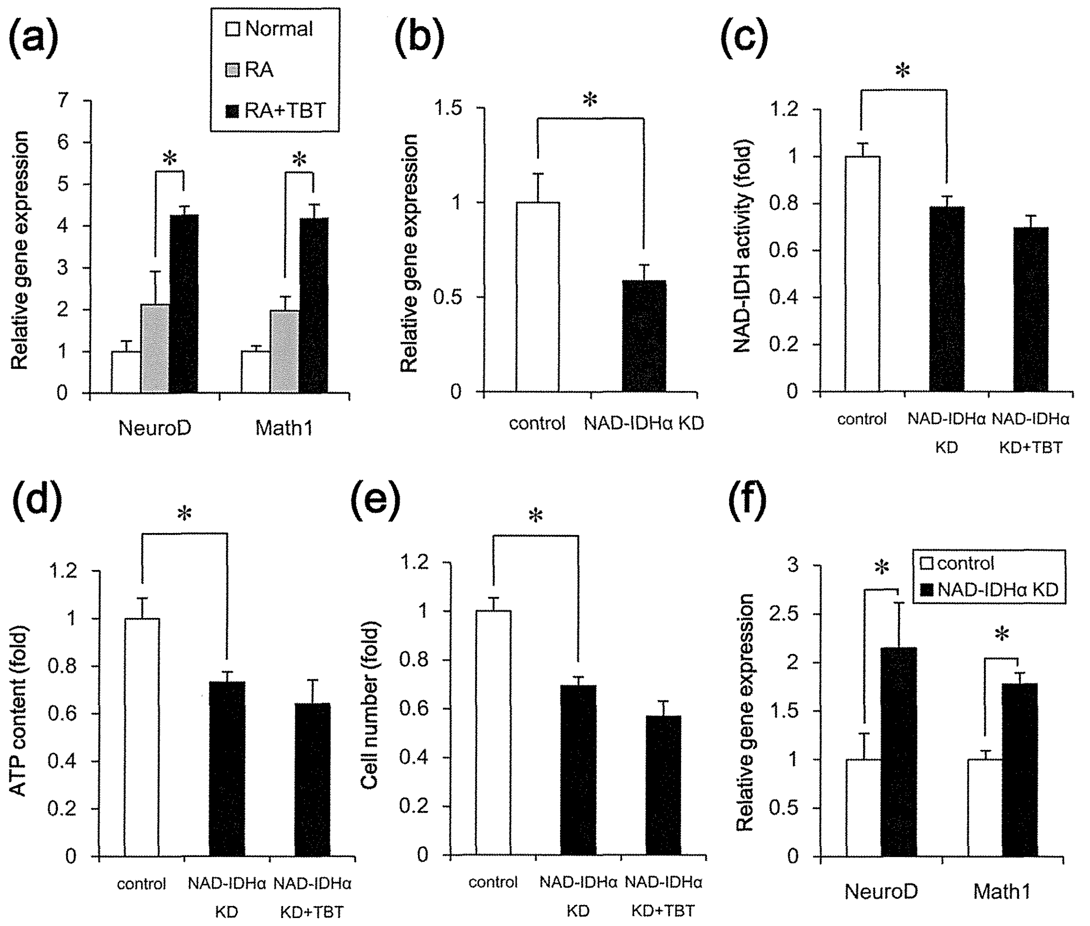

Figure 3 | Effect of TBT exposure or NAD-IDH knockdown on neuronal differentiation in RA-treated NT2/D1 cells. (a) After treatment with RA for 7 days, the cells were treated with RA in the presence of 100 nM TBT for an additional 7 days. The relative expression levels of the neuronal markers NeuroD and Math1 were measured using real-time PCR. The relative changes were determined following normalization to the levels of RPL13. (b–e) The cells were infected with lentiviruses containing a vector encoding a shRNA directed against NAD-IDHα or a scrambled sequence shRNA (control). The infected cells were subjected to selection with 0.5 μg/ml puromycin for 72 h and were then exposed to TBT at 100 nM for 24 h. (b) The relative expression of NAD-IDHα was measured using real-time PCR. The relative change in expression was normalized to the levels of RPL13. (c) NAD-IDH activity was determined in the lysed cells. (d) The intracellular ATP content was determined in the lysed cells. (e) Infected cells were seeded into 100 mm dishes and cultured for 24 h. Cell count was determined using a hemocytometer. (f) After treatment with RA for 7 days, followed by treatment with RA and the shRNA-containing lentiviruses for an additional 7 days, the relative expression levels of the neuronal markers NeuroD and Math1 were measured using real-time PCR. The relative changes were determined following normalization to the levels of RPL13. * $P < 0.05$ compared with the corresponding group.

quitously expressed, the toxicity of TBT might be observed in various cell types. Several TCA cycle enzymes have been reported to contribute to cell proliferation. For example, NADP-IDH plays a role for cell growth under hypoxic conditions in human glioblastoma cells[26]. Another study has shown that aconitase mediated cell proliferation via ATP production in human prostate carcinoma cells[27]. NAD-IDH has been shown to regulate the metabolic fluxes and the generation of ATP in the TCA cycle[28]. Therefore, it is likely that NAD-IDH is a target of TBT cytotoxicity and regulates cell growth in embryonic carcinoma cells.

In addition to cell growth inhibition, we also showed that neural differentiation is enhanced by TBT exposure or NAD-IDH inhibition (Figure 3). Consistent with our data, overexpression of NAD-IDHα has been shown to reduce neuronal differentiation and neurite outgrowth through the inactivation of MAPK phosphorylation in PC12 cells[29]. Because TBT exposure has been reported to induce neurotoxicity via ERK and p38MAPK phosphorylation in cultured rat cortical neurons[30], TBT exposure might cause cytotoxicity through the MAPK pathways. Thus, a non-genomic pathway plays a role in TBT toxicity. Indeed, the genomic target PPARγ and treatment with cycloheximide did not alter the effects of TBT (Figure S1–3). It is unlikely that transcriptional regulation is involved in NAD-IDH activity and the enhancement of neuronal differentiation. The downstream pathway of TBT-NAD-IDH should be determined in embryonic carcinoma cells.

Our data suggest that TBT regulates NAD-IDH activity through possible interaction. However, we can not conclude that it is through direct binding. Previous reports have suggested that TBT can bind to multiple target proteins, such as PPARγ, RXR, F1F0 ATP synthase and 11β-hydroxysteroid dehydrogenase (11β-HSD) type 2, with broad specificity[19,31]. For example, TBT binds the RXRα ligand-binding domain through a covalent bond between the tin atom and the Cys residue[32]. TBT also binds 11β-HSD type 2 by interacting with several Cys residues in the active site[31]. Because the ligand-binding pocket of hNAD-IDHα contains several Cys residues[33] and has enough space to accommodate TBT, TBT might bind to hNAD-IDHα via Cys residues. Future conformational analysis, including X-ray crystallography or computer simulation, and mutagenesis studies should be performed to determine whether TBT binds to hNAD-IDHα or not.

Our metabolomic analysis showed that TBT inhibited cell growth and enhanced neuronal differentiation through possible direct

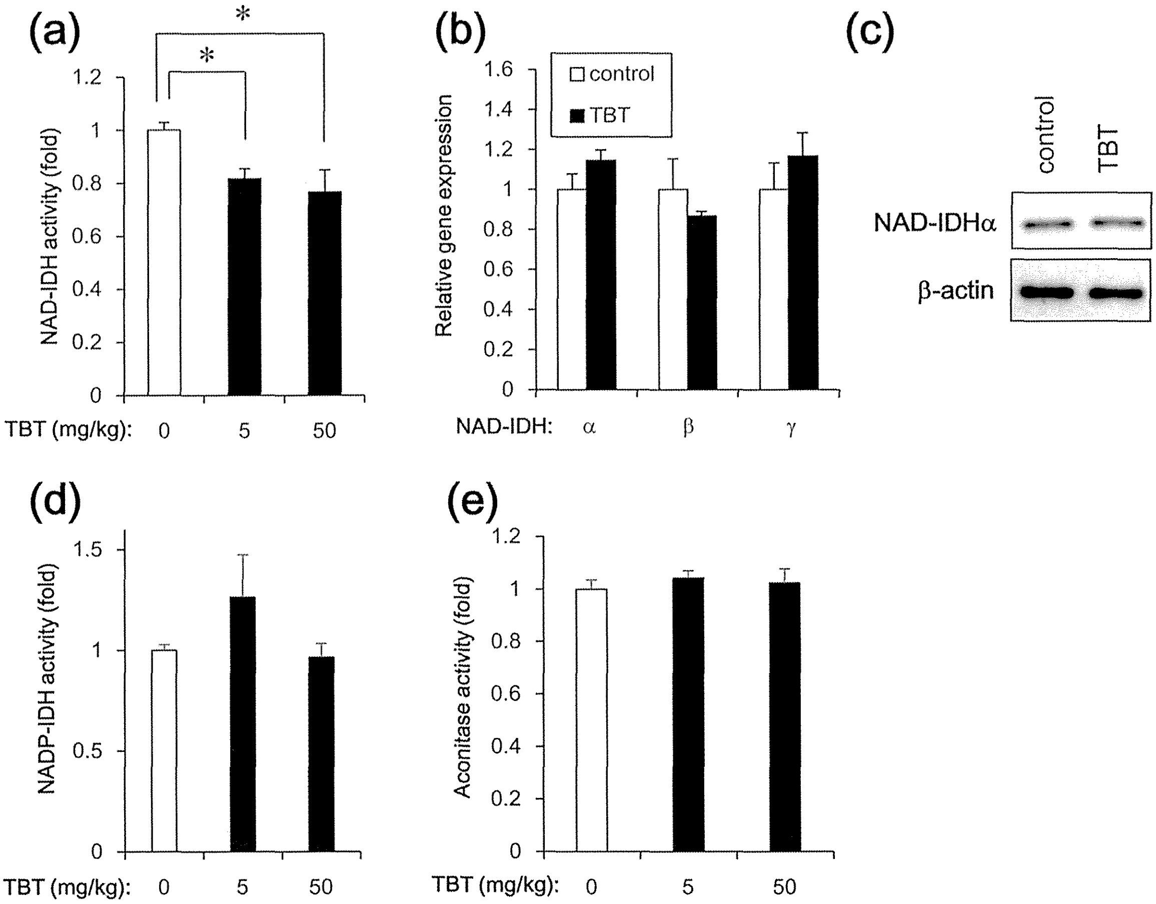

Figure 4 | NAD-IDH enzyme activity in the brain of rats orally exposed to TBT at doses of 5 and 50 mg/kg for 6 h. (a) NAD-IDH activity was determined in the brain lysates. (b) The relative expression levels of NAD-IDHα, β, and γ in rats exposed to 50 mg/kg TBT were measured using real-time PCR. The relative changes were normalized to the levels of RPL13. (c) The expression of NAD-IDHα protein was examined by western blot analysis using the anti-NAD-IDHα and anti-β-actin antibodies. Cropped blots were shown and the full-length blots were indicated in Supplementary Fig. 4. (d) NADP-IDH activity was determined in the brain lysates. (e) Aconitase activity was determined in the brain lysates. * $P < 0.05$ compared with the corresponding TBT 0 group.

inhibition of NAD-IDH activity in human embryonic carcinoma cells. Thus, comprehensive approach of non-genomic metabolic pathway might be a powerful tool to elucidate the mechanism of EDC action.

Methods

Chemicals and reagents. TBT was obtained from Tokyo Chemical Industry (Tokyo, Japan). Tin acetate (TA) and rosiglitazone were obtained from Sigma-Aldrich (St. Louis, MO, USA). All other reagents were of analytical grade and were obtained from commercial sources.

Cell culture. NT2/D1 cells were obtained from the American Type Culture Collection. The cells were cultured in Dulbecco's modified Eagle's medium (DMEM; Sigma-Aldrich) supplemented with 10% fetal bovine serum (FBS; Biological Industries, Ashrat, Israel) and 0.05 mg/ml penicillin-streptomycin mixture (Life Technologies, Carlsbad, CA, USA) at 37°C and 5% CO2. For neural differentiation, all-trans retinoic acid (RA; Sigma-Aldrich) was added to the medium twice a week at a final concentration of 10 μM.

Determination of TCA cycle metabolites. Intracellular metabolites were extracted and used for subsequent capillary electrophoresis time-of-flight mass spectrometry (CE-TOFMS) analysis, as previously described. The amounts of the metabolites were determined using an Agilent CE capillary electrophoresis system (Agilent Technologies, Waldbronn, Germany) equipped with an Agilent G3250AA LC/MSD TOF system (Agilent Technologies, Palo Alto, CA), an Agilent 1100 series isocratic HPLC pump, a G1603A Agilent CE-MS adapter kit, and a G1607A Agilent CE-electrospray ionization 53-MS sprayer kit. For system control and data acquisition, the G2201AA Agilent ChemStation software was used for CE, and the Agilent TOF (Analyst QS) software was used for the TOFMS.

Measurement of intracellular ATP levels. The intracellular ATP content was measured using the ATP Determination Kit (Life Technologies), according to the manufacturer's protocol. Briefly, the cells were washed and lysed with 0.1% Triton X-100/PBS. The resulting cell lysates were added to a reaction mixture containing 0.5 mM D-luciferin, 1 mM DTT, and 1.25 μg/ml luciferase and incubated for 30 min at room temperature. Luminescence was measured using a Wallac1420ARVO fluoroscan (Perkin-Elmer, Waltham, MA, USA). The luminescence intensities were normalized to the total protein content.

Isocitrate dehydrogenase (IDH) activity assay. IDH activity was determined using the commercial Isocitrate Dehydrogenase Activity Colorimetric Assay Kit (Biovision, Mountain View, CA, USA), according to the manufacturer's instructions. Briefly, NT2/D1 cells were lysed in an assay buffer provided in the kit. The lysate was centrifuged at 14,000 g for 15 min, and the cleared supernatant was used for the assay. NADP or NAD was used as the substrate for the NADP-IDH or NAD-IDH assay, respectively.

Real-time PCR. Total RNA was isolated from NT2/D1 cells using the TRIzol reagent (Life Technologies), and quantitative real-time reverse transcription (RT)-PCR with the QuantiTect SYBR Green RT-PCR Kit (QIAGEN, Valencia, CA, USA) was performed using an ABI PRISM 7900HT sequence detection system (Applied Biosystems, Foster City, CA, USA), as previously reported. The relative changes in the transcript amounts of each sample were normalized to the mRNA levels of ribosomal protein L13 (RPL13). The following primer sequences were used for real-time PCR analysis: human NAD-IDHα: forward, 5′-ATCGGAGGTCTCGGTGTG-3′, reverse, 5′-AGGAGGGCTGTGGGATTC-3′; human NAD-IDHβ: forward, 5′-GCCTC-AGCCGCATATCATAG-3′, reverse, 5′-GAGCAGGTGCTGAGTTCCAT-3′; human NAD-IDHγ: forward, 5′-TTAGCGGACGGAGGAATTGT-3′, reverse, 5′-CAGCCCTTCTCTGCCGT-3′; human NeuroD: forward, 5′-GGAAACGA-ACCCACTGTGCT-3′, reverse, 5′-GCCACACCAAATTCGTGGTG-3′; human Math1: forward, 5′-GTCCGAGCTGCTACAAACG-3′, reverse, 5′-GTGGTGGT-GGTCGCTTTT-3′; human RPL13: forward, 5′-CATCGTGGCTAAACAGGTAC-

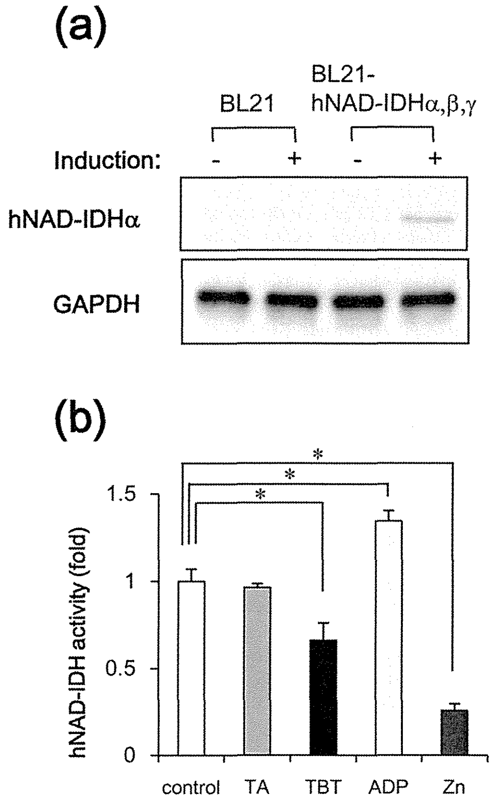

Figure 5 | Reduction of NAD-IDH enzyme activity by interaction with TBT in an E. coli expression system. (a) After the expression of pHIDHα, β, γ was induced by culturing E. coli BL21 transformants at 25°C for 20 h, crude extracts were prepared and were subjected to western blot analysis using the anti-NAD-IDHα and anti-GAPDH antibodies. Cropped blots were shown and the full-length blots were indicated in Supplementary Fig. 4. (b) After treatment with 100 nM TBT for 1 h, NAD-IDH activity was determined in the crude extracts. ADP (100 μM) and Zn^{2+} (2 mM) were used as positive and negative controls, respectively. * $P < 0.05$ compared with the corresponding control group.

TG-3′, reverse, 5′-GCACGACCTTGAGGGCAGCC-3′; rat NAD-IDHα: forward, 5′-TGGGTGTCCAAGGTCTCTC-3′, reverse, 5′-CTCCCACTGAATAGGTG-CTTTG-3′; rat NAD-IDHβ: forward, 5′-AGGCACAAGATGTGAGGGTG-3′, reverse, 5′-CAGCAGCCTTGAACACTTCC-3′; rat NAD-IDHγ: forward, 5′-TGGGCGGCATACAGTGACTA-3′, reverse, 5′-TTGGAGCTTACATGCAC-CTCT-3′; rat RPL13: forward, 5′-GGCTGAAGCCTACCAGAAAG-3′, reverse, 5′-CTTTGCCTTTTCCTTCCGTT-3′.

Aconitase activity assay. Aconitase activity was determined using the commercial Aconitase Activity Colorimetric Assay Kit (Biovision), according to the manufacturer's instructions. Briefly, NT2 cells were lysed in an assay buffer provided in the kit. The lysate was centrifuged at 14,000 g for 15 min, and the cleared supernatant was used for the aconitase assay.

NAD-IDHα knockdown experiment. Transient gene knockdown was performed using NAD-IDHα shRNA lentiviruses from Sigma-Aldrich (MISSION® shRNA) according to manufacturer's protocol. A scrambled hairpin sequence was used as a negative control. Briefly, the cells were infected with the viruses at a multiplicity of infection of 10, in the presence of 8 μg/ml hexadimethrine bromide (Sigma-Aldrich), for 24 h, and were then subjected to selection with 0.5 μg/ml puromycin for 72 h prior to functional analyses.

Tissue preparation. The present study was approved by the animal ethics committee and was conducted in accordance with the regulations on the use of living modified organisms of Hiroshima University. Male Slc:Wistar/ST rats (8 weeks old) were purchased from Japan SLC, Inc. (Shizuoka, Japan). They were housed under controlled temperature, 12 h light/dark cycle, and humidity (75 ± 5%) for at least 1 week prior to experiments. Standard pellet food and water were provided ad libitum. TBT solution (5 and 50 mg/kg body weight) was orally administered to rats. TBT was dissolved in polyethylene glycol. The whole brain was exposed by the use of fine scissors and forceps, and the frontal part of cerebral cortex was excised from the brain.

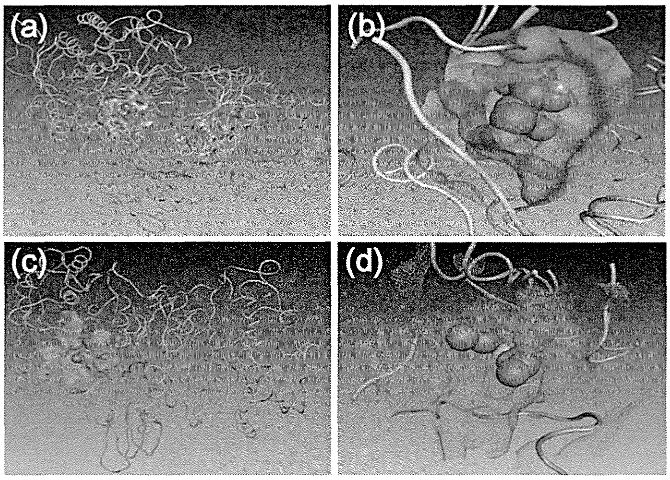

Figure 6 | In silico docking simulation analysis. (a) Overlaid structures of the calculated hNAD-IDHα (orange) and hNADP-IDH (cyan) homodimers bound to isocitric acid (Space-filling model). (b) The ligand binding pockets of the hNAD-IDHα (solid) and hNADP-IDH (wireframe) proteins. (c, d) Docking structure of hNAD-IDHα containing TBT (Space-filling model).

Transformation and Expression of Recombinant Human NAD-IDH Proteins in E. coli. pHIDHαβ1γ plasmid DNA (a kind gift from Dr. T. L. Huh) was used to transform E. coli BL21 (DE3) ultracompetent cells (BioDynamics, Tokyo, Japan). The colonies with positive inserts were subcultured and grown overnight at 37°C in LB medium (2 ml) supplemented with ampicillin (0.1 mg/ml). To express the enzyme, 15 ml tubes containing 2 ml of LB medium with 0.1 mg/ml ampicillin were inoculated with freshly grown E. coli cells (1% v/v), and these cultures were grown at 37°C while being shaken at 220 rpm for 4 h. The flasks were then temporarily placed in chilled water to lower the culture temperature to 25°C. Protein expression was induced in the cells by shaking at a lower speed of 140 rpm with minimal aeration at 25°C for 20 h. Then, 2 ml of the cell culture was centrifuged at 6,000 g for 15 min to separate the cells from the media, and the pellet was suspended in a total volume of 300 μl of cold assay buffer, a component of Isocitrate Dehydrogenase Activity Assay Kit. The suspended cells were subjected to 3 cycles of freeze-thaw before sonication (5 cycles of 15 sec sonication and 45 sec rest) and lysed. The cell lysate was centrifuged at 14,000 g for 15 min, and the cleared supernatant (crude extract) was separated. Recombinant human NAD-IDH activity was determined by subtracting basal activity in the crude extract from control BL21 cells.

Western blot analysis. Western blot analysis was performed as previously reported[34]. Briefly, the cells were lysed with Cell Lysis Buffer (Cell Signaling Technology, Danvers, MA, USA), and the proteins were separated by sodium dodecyl sulfate (SDS)-polyacrylamide gel electrophoresis and electrophoretically transferred to Immobilon-P (Millipore, Billerica, MA, USA). The membranes were probed with an anti-NAD-IDH (IDH3) α polyclonal antibody (1 : 1,000; Abcam, Cambridge, UK), an anti-β-actin monoclonal antibody (1 : 5,000; Sigma-Aldrich), and an anti-GAPDH monoclonal antibody (1 : 2,000; Abcam). The membranes were then incubated with secondary antibodies against rabbit or mouse IgG conjugated to horseradish peroxidase (Cell Signaling Technology). The bands were visualized using the ECL Western Blotting Analysis System (GE Healthcare, Buckinghamshire, UK), and the images were acquired using a LAS-3000 Imager (FUJIFILM UK Ltd., Systems, Bedford, UK). The density of each band was quantified using the ImageJ software (NIH, Bethesda, MD, USA).

In silico docking simulation studies. Homology modeling and docking studies of the human NAD-IDHα (hNAD-IDHα) and NADP-IDH (hNADP-IDH) homodimers were performed using Molecular Operating Environment (MOE) 2012.10. The models of hNAD-IDHα and hNADP-IDH were constructed based on the crystallographic structure of the porcine NADP-IDH homodimer (PDB: 1LWD)[35] using the standard protocols in MOE 2012.10. The docking simulations of the TBT-bound hNAD-IDHα and hNADP-IDH were carried out using ASEDock[36]. The TBT ligand was assigned in ASEDock, and the conformations were calculated using MMFF94S force field[37].

Statistical analysis. Results are shown as mean ± S.D. Statistical analysis was performed using one-way ANOVA followed by Dunnett's test. Differences at $P < 0.05$ were considered to be significant.

1. Toppari, J. *et al.* Male reproductive health and environmental xenooestrogens. *Environ. Health Perspect.* **104**, 741–803 (1996).

2. Hall, J. M. & Korach, K. S. Analysis of the molecular mechanisms of human estrogen receptors alpha and beta reveals differential specificity in target promoter regulation by xenoestrogens. *J. Biol. Chem.* **277**, 44455–44461 (2002).
3. Newbold, R. R., Padilla-Banks, E. & Jefferson, W. N. Adverse Effects of the Model Environmental Estrogen Diethylstilbestrol Are Transmitted to Subsequent Generations. *Endocrinology* **147**, s11–17 (2006).
4. Bulayeva, N. N., Gametchu, B. & Watson, C. S. Quantitative measurement of estrogen-induced ERK 1 and 2 activation via multiple membrane-initiated signaling pathways. *Steroids* **69**, 181–192 (2004).
5. Liu, D., Homan, L. L. & Dillon, J. S. Genistein acutely stimulates nitric oxide synthesis in vascular endothelial cells by a cyclic adenosine 5′-mono-phosphate-dependent mechanism. *Endocrinology* **145**, 5532–5539 (2004).
6. Watson, C. S., Alyea, R. A., Jeng, Y. J. & Kochukov, M. Y. Nongenomic actions of low concentration estrogens and xenoestrogens on multiple tissues. *Mol. Cell Endocrinol.* **274**, 1–7 (2007).
7. Bredfeldt, T. G. *et al.* Xenoestrogen-induced regulation of EZH2 and histone methylation via estrogen receptor signaling to PI3K/AKT. *Mol. Endocrinol.* **24**, 993–1006 (2010).
8. Gardlund, A. T. *et al.* Effects of prenatal exposure to tributyltin and trihexyltin on behavior in rats. *Neurotoxicol. Teratol.* **13**, 99–105 (1991).
9. Noda, T. *et al.* Teratogenicity study of tri-n-butyltin acetate in rats by oral administration. *Toxicol. Lett.* **55**, 109–115 (1991).
10. Whalen, M. M., Loganathan, B. G. & Kannan, K. Immunotoxicity of environmentally relevant concentrations of butyltins on human natural killer cells in vitro. *Environ Res.* **81**, 108–116 (1999).
11. Matthiessen, P. & Gibbs, P. E. Critical appraisal of the evidence for tributyltin mediated endocrine disruption in mollusks. *Environ. Toxicol. Chem.* **17**, 37–43 (1998).
12. McAllister, B. G. & Kime, D. E. Early life exposure to environmental levels of the aromatase inhibitor tributyltin causes masculinisation and irreversible sperm damage in zebrafish (Danio rerio). *Aquat. Toxicol.* **65**, 309–316 (2003).
13. Nishikawa, J. *et al.* Involvement of the retinoid X receptor in the development of imposex caused by organotins in gastropods. *Environ. Sci. Technol.* **38**, 6271–6276 (2004).
14. Kanayama, T., Kobayashi, N., Mamiya, S., Nakanishi, T. & Nishikawa, J. Organotin compounds promote adipocyte differentiation as agonists of the peroxisome proliferator-activated receptor gamma/retinoid X receptor pathway. *Mol. Pharmacol.* **67**, 766–774 (2005).
15. Grün, F. *et al.* Endocrine-disrupting organotin compounds are potent inducers of adipogenesis in vertebrates. *Mol. Endocrinol.* **20**, 2141–2155 (2006).
16. Cooke, G. M. Effect of organotins on human aromatase activity in vitro. *Toxicol. Lett.* **126**, 121–130 (2002).
17. Doering, D. D., Steckelbroeck, S., Doering, T. & Klingmüller, D. Effects of butyltins on human 5alpha-reductase type 1 and type 2 activity. *Steroids* **67**, 859–867 (2002).
18. McVey, M. J. & Cooke, G. M. Inhibition of rat testis microsomal 3beta-hydroxysteroid dehydrogenase activity by tributyltin. *J. Steroid Biochem. Mol. Biol.* **86**, 99–105 (2003).
19. von Ballmoos, C., Brunner, J. & Dimroth, P. The ion channel of F-ATP synthase is the target of toxic organotin compounds. *Proc. Natl. Acad. Sci. U S A* **101**, 11239–11244 (2004).
20. Yamada, S., Kotake, Y., Sekino, Y. & Kanda, Y. AMP-activated protein kinase-mediated glucose transport as a novel target of tributyltin in human embryonic carcinoma cells. *Metallomics* **5**, 484–491 (2013).
21. Vinekar, R., Verma, C. & Ghosh, I. Functional relevance of dynamic properties of Dimeric NADP-dependent Isocitrate Dehydrogenases. *BMC Bioinformatics* **13**, S2 (2012).
22. Birket, M. J. *et al.* A reduction in ATP demand and mitochondrial activity with neural differentiation of human embryonic stem cells. *J. Cell Sci.* **124**, 348–358 (2011).
23. Kim, Y. O. *et al.* Identification and functional characterization of a novel, tissue-specific NAD(+)-dependent isocitrate dehydrogenase β subunit isoform. *J. Biol. Chem.* **274**, 36866–36875 (1999).
24. Cohen, P. F. & Colman, R. F. Diphosphopyridine nucleotide dependent isocitratedehydrogenase from pig heart. Charactgerization of the active substrate and modes of regulation. *Biochemistry* **11**, 1501–1508 (1972).
25. Lemire, J., Mailloux, R. & Appanna, V. D. Zinc toxicity alters mitochondrial metabolism and leads to decreased ATP production in hepatocytes. *J. Appl. Toxicol.* **28**, 175–182 (2008).
26. Wise, D. R. *et al.* Hypoxia promotes isocitrate dehydrogenase-dependent carboxylation of α-ketoglutarate to citrate to support cell growth and viability. *Proc. Natl. Acad. Sci. U S A* **108**, 19611–19616 (2011).
27. Juang, H. H. Modulation of mitochondrial aconitase on the bioenergy of human prostate carcinoma cells. *Mol. Genet. Metab.* **81**, 244–252 (2004).
28. Gabriel, J. L., Zervos, P. R. & Plaut, G. W. Activity of purified NAD-specific isocitrate dehydrogenase at modulator and substrate concentrations approximating conditions in mitochondria. *Metabolism* **35**, 661–667 (1986).
29. Cho, S. A. *et al.* Up-regulation of Idh3alpha causes reduction of neuronal differentiation in PC12 cells. *BMB Rep.* **43**, 369–374 (2010).
30. Nakatsu, Y. *et al.* Glutamate excitotoxicity is involved in cell death caused by tributyltin in cultured rat cortical neurons. *Toxicol. Sci.* **89**, 235–242 (2006).
31. Atanasov, A. G., Nashev, L. G., Tam, S., Baker, M. E. & Odermatt, A. Organotins disrupt the 11beta-hydroxysteroid dehydrogenase type 2-dependent local inactivation of glucocorticoids. *Environ. Health Perspect.* **113**, 1600–1606 (2005).
32. le Maire, A. *et al.* Activation of RXR-PPAR heterodimers by organotin environmental endocrine disruptors. *EMBO Rep.* **10**, 367–373 (2009).
33. Kim, Y. O. *et al.* Characterization of a cDNA clone for human NAD(+)-specific isocitrate dehydrogenase alpha-subunit and structural comparison with its isoenzymes from different species. *Biochem. J.* **308**, 63–68 (1995).
34. Kanda, Y. & Watanabe, Y. Adrenaline increases glucose transport via a Rap1-p38MAPK pathway in rat vascular smooth muscle cells. *Br. J. Pharmacol.* **151**, 476–482 (2007).
35. Ceccarelli, C., Grodsky, N. B., Ariyaratne, N., Colman, R. F. & Bahnson, B. J. Crystal structure of porcine mitochondrial NADP$^+$-dependent isocitrate dehydrogenase complexed with Mn^{2+} and isocitrate. Insights into the enzyme mechanism. *J. Biol. Chem.* **277**, 43454–43462 (2002).
36. Goto, J., Kataoka, R., Muta, H. & Hirayama, N. ASEDock-docking based on alpha spheres and excluded volumes. *J. Chem. Inf. Model.* **48**, 583–590 (2008).
37. Halgren, T. A. MMFF VI. MMFF94s option for energy minimization studies. *J. Comput. Chem.* **20**, 720–729 (1999).

Acknowledgments

We thank Ms. Mami Kohno, Mr. Kyoichi Masuda, and Ms. Saki Tanaka (Graduate School of Biomedical and Health Sciences, Hiroshima University) for technical assistance in the animal experiment. This work was supported by a Grant-in-Aid for Scientific Research from the Ministry of Education, Culture, Sports, Science, and Technology, Japan (#23590322 to Y.K.), a Health and Labour Sciences Research Grant from the Ministry of Health, Labour and Welfare, Japan (Y.K.), and a grant from the Smoking Research Foundation (Y.K.).

Author contributions

S.Y. performed most of the experiments. Y.Ka. planned the project. S.Y., Y.S. and Y.Ka. wrote the manuscript. Y.Ko. performed the animal experiments. Y.D. and M.K. performed *In silico* docking simulation analysis. All authors reviewed the manuscript.

Additional information

Supplementary information accompanies this paper at http://www.nature.com/scientificreports

Competing financial interests: The authors declare no competing financial interests.

How to cite this article: Yamada, S. *et al.* NAD-dependent isocitrate dehydrogenase as a novel target of tributyltin in human embryonic carcinoma cells. *Sci. Rep.* **4**, 5952; DOI:10.1038/srep05952 (2014).

This work is licensed under a Creative Commons Attribution-NonCommercial-NoDerivs 4.0 International License. The images or other third party material in this article are included in the article's Creative Commons license, unless indicated otherwise in the credit line; if the material is not included under the Creative Commons license, users will need to obtain permission from the license holder in order to reproduce the material. To view a copy of this license, visit http://creativecommons.org/licenses/by-nc-nd/4.0/

Cellular localization and dendritic function of rat isoforms of the SRF coactivator MKL1 in cortical neurons

Mitsuru Ishikawa[a,*], Jun Shiota[a,*], Yuta Ishibashi[a,*], Tomoyuki Hakamata[a,*], Shizuku Shoji[a], Mamoru Fukuchi[a], Masaaki Tsuda[a], Tomoaki Shirao[b], Yuko Sekino[c], Jay M. Baraban[d] and Akiko Tabuchi[a]

The ability of megakaryoblastic leukemia 1 (MKL1) to function as a serum response factor (SRF) coactivator is regulated through its association with G-actin. In the cytoplasm, MKL1 binds to G-actin through RPXXXEL (RPEL) motifs. However, dissociation of MKL1 from G-actin triggers its translocation into the nucleus where it stimulates SRF-mediated gene expression. Previous characterization of rat MKL1 gene products has identified several isoforms: full-length MKL1, basic, SAP, and coiled-coil domain (BSAC), MKL1-elongated derivative of yield (MELODY), and MKL1met. In this study, we have investigated whether these MKL1 isoforms, which contain different numbers of RPEL motifs, differ in their subcellular localization, transcriptional activity, and effect on dendritic number and axonal length. Immunofluorescent staining of cultured cortical neurons expressing individual FLAG-tagged MKL1 isoforms indicated that all MKL1 isoforms are present in both the cytoplasm and the nucleus. However, MKL1met, which contains two RPEL motifs, shows enhanced nuclear staining compared with the other three isoforms, full-length MKL1, basic, SAP, and coiled-coil domain, and MKL1-elongated derivative of yield, which contain three RPEL motifs. Consistent with its preferential nuclear localization, overexpression of MKL1met, but not other isoforms, increases SRF-mediated transcriptional responses and reduces the number of dendrites. In contrast to the inhibitory effect of MKL1met on dendritic number, axonal length is not affected by overexpression of any of the MKL1 isoforms. These findings suggest that the subcellular localization of MKL1 isoforms, which is mediated by the number of actin-binding RPEL motifs, regulates their effect on SRF-mediated gene expression and dendritic morphology. *NeuroReport* 25:585–592 © 2014 Wolters Kluwer Health | Lippincott Williams & Wilkins.

NeuroReport 2014, **25**:585–592

Keywords: dendritic morphology, gene expression, megakaryoblastic leukemia, serum response factor

[a]Laboratory of Molecular Neurobiology, Graduate School of Medicine and Pharmaceutical Sciences, University of Toyama, Toyama, [b]Department of Neurobiology and Behavior, Gunma University, Graduate School of Medicine, Maebashi, [c]Division of Pharmacology, Biological Safety Research Center, National Institute of Health Sciences, Tokyo, Japan and [d]Solomon H. Snyder Department of Neuroscience, Johns Hopkins University, School of Medicine, Baltimore, Maryland, USA

Correspondence to Akiko Tabuchi, Laboratory of Molecular Neurobiology, Graduate School of Medicine and Pharmaceutical Sciences, University of Toyama, 2630 Sugitani, Toyama 930-0194, Japan
Tel: +81 76 434 7536; fax: +81 76 434 5048;
e-mail: atabuchi@pha.u-toyama.ac.jp

*Mitsuru Ishikawa, Jun Shiota, Yuta Ishibashi, and Tomoyuki Hakamata equally contributed to the writing of this article.

Received 28 November 2013 **accepted** 4 February 2014

Introduction

Serum response factor (SRF) plays critical roles in pathological and biological processes including brain development and function [1–6]. SRF-mediated gene expression is tightly regulated by SRF binding cofactors, which are classified into at least two families. One family contains the Ets-like transcription factor (Elk1), SRF accessory protein 1 (SAP1)/Elk4, and a newly described Ets transcription factor (Net)/Ets-related protein/SAP2/Elk3 [6]. The other, referred to as the myocardin and megakaryoblastic leukemia (MKL) family, consists of megakaryocytic acute leukemia/MKL1/myocardin-related transcription factor-A/basic SAP and coiled-coil domain (BSAC) and MKL2/MRTF-B [7–11]. The ability of MKL1 to bind to G-actin through its RPXXXEL (RPEL) motifs plays a prominent role in restraining its transcriptional activity. Conversely, actin rearrangement can lead to its dissociation from G-actin allowing it to translocate into the nucleus [12,13]. Accumulating evidence suggests that MKL1 and MKL2 are enriched in the brain [14] and are deeply involved in regulating neuronal migration and morphology [14,15]. Therefore, analyzing the expression and function of MKL family members in neurons might provide novel insights into the impact of SRF-mediated transcription on neuronal morphology and function.

Use of alternative 5′-exons and translation start sites on the MKL1 gene gives rise to multiple MKL1 isoforms [8,12]. Previously, we identified several rat MKL1 transcripts, including full-length MKL1 (FLMKL1), BSAC, and a novel isoform, MKL1-elongated derivative of yield (MELODY), each of which uses a distinct 5′-exon [16]. These three transcripts are enriched in the testis and brain and are differentially regulated during

---

Supplemental digital content is available for this article. Direct URL citations appear in the printed text and are provided in the HTML and PDF versions of this article on the journal's website (*www.neuroreport.com*).

0959-4965 © 2014 Wolters Kluwer Health | Lippincott Williams & Wilkins DOI: 10.1097/WNR.0000000000000141

Copyright © Lippincott Williams & Wilkins. Unauthorized reproduction of this article is prohibited.

brain development [16]. The deduced exon–intron organization, domain structure, and different N-termini of rat MKL1 transcripts are illustrated in supplementary Fig. 1 (Supplemental Digital Content 1, *http://links.lww.com/WNR/A275*) [16]. Although the N-terminal regions just ahead of the first RPEL motifs are different between BSAC and MELODY, these two transcripts encode proteins that contain three RPEL motifs (Supplementary Fig. 1B and C, Supplemental Digital Content 1, *http://links.lww.com/WNR/A275*) [16]. In contrast, two isoforms are generated from the FLMKL1 transcript through the use of two alternative translational start sites: the upstream site (CTG) yields the FLMKL1 isoform, which has three RPEL motifs, whereas the downstream start site (ATG) yields MKL1met, which contains only two RPEL motifs (Supplementary Fig. 1B and C, Supplemental Digital Content 1, *http://links.lww.com/WNR/A275*) [12,16]. As RPEL motifs bind to G-actin, it is possible that the number of RPEL motifs affect nucleocytoplasmic localization or function of MKL1. In this study, we expressed these four MKL1 isoforms in rat cortical neurons to compare their subcellular localization and impact on SRF-mediated transcription and neuronal morphology.

Materials and methods

Animals

Neurons of pregnant Sprague–Dawley rats used to prepare primary neuronal cultures were purchased from Sankyo Labo Service Corporation Inc. (Tokyo, Japan). All experiments were carried out in accordance with the guidelines of the Animal Care and Experimental Committee of the University of Toyama, Sugitani Campus. The protocols were approved. Every effort was made to minimize suffering, including anesthetizing with pentobarbital (50 mg/kg, intraperitoneal injection).

Plasmids and antibodies

Construction of FLAG-tagged rat MKL1 vectors (FLAG-FLMKL1, FLAG-BSAC, FLAG-MELODY, and FLAG-MKL1met) has been described previously [16]. The expression vector for enhanced green fluorescent protein (GFP; pEGFP-C1) was purchased from Clontech (Mountain View, California, USA). The SRF reporter vector, 3DA-Luc, was generously supplied by Dr R. Treisman (Cancer Research Institute, London, UK) [12,17,18]. The CRE-reporter vector, pCRE-Luc (CRE-Luc), and the SRE reporter vector, pSRE-Luc (SRE-Luc), were purchased from Stratagene (La Jolla, California, USA). An internal control vector, RSV-βgal vector, has been described previously [14].

The following antibodies were used at the indicated dilutions: Alexa Fluor 488 or 594-conjugated anti-rabbit IgG (Life Technologies, Carlsbad, California, USA, A-11008 and A-11012, respectively; 1 : 1000) and Alexa Fluor 488 or 594-conjugated anti-mouse IgG (Life Technologies, A-11001 and A-11005, respectively; 1 : 1000) produced in goats. The following rabbit polyclonal antibodies were used: anti-GFP (Life Technologies, A-11122 or Medical and Biological Laboratories, 598; 1 : 500 or 1 : 1000). The following mouse monoclonal antibodies were used: anti-FLAG (Sigma, St Louis, Missouri, USA, F3165; 1 : 1000), anti-Tau-1 (Chemicon, Temecula, California, USA, MAB3420; 1 : 1000), and anti-MAP2 (Sigma, M4403; 1 : 1000).

Cell culture

Dissociated cortical cell cultures were prepared from rat embryos at embryonic day 17 as described previously [14]. For reporter assays, cells were plated at 2×10^6 cells/well in six-well plates coated with poly-D-lysine (Sigma). For dendritic morphological assays, cells were seeded at a density of $\sim 7 \times 10^5$ cells/well onto 18-mm circular coverslips coated with poly-D-lysine that had been placed in 12-well plates. For measurement of axonal length, cells were seeded onto coverslips as described above at a density of $\sim 3.0 \times 10^5$ cells/well.

Transfection into rat cortical neurons

For analyzing transcriptional activity, cellular localization, and dendritic morphology, rat cortical neurons cultured for 7 days were transfected using the calcium phosphate precipitation method as described previously [14]. According to our previous observation of the expression levels of FLAG-tagged MKL1 isoforms in NIH3T3 cells [16], we adjusted the amounts of the expression vectors used for transfection of neuronal cultures (see figure legends for specific amounts used for each of these plasmids). We evaluated the expression levels by comparing band intensities on western blotting and observed the same expression levels when the ratio of the expression vectors for transfection was empty vector : FLMKL1 : BSAC : MELODY : MKL1met = 2 : 1 : 2 : 1 : 1.5 [16]. The transfection efficiencies of all samples were equal, as the expression of the internal control GFP, which was cotransfected with the FLAG-tagged expression vector, was equal [16].

Immunostaining

The procedures used to process cortical cultures for immunostaining have been described previously [14]. In this experiment, fluoromount (Diagnostic BioSystems, Pleasanton, California, USA) was used to mount coverslips containing cortical cultures onto microscope slides.

Localization of FLAG-tagged MKL1

After immunostaining, immunofluorescence images were acquired using a Zeiss LSM700 confocal microscope (Zeiss, Oberkochen, Germany). Thereafter, the fluorescence intensities of FLAG-MKL1 isoforms in the cytoplasm and the nucleus were measured using LSM Software ZEN (Zeiss). The cytoplasmic signal was captured as the FLAG-derived immunoreactivity in the GFP-positive and 4′,6-diamidino-2-phonylindole (DAPI)-negative areas and the nuclear signal was captured as the FLAG-derived immunoreactivity in the GFP and DAPI double-positive areas. Twenty neurons were examined

Copyright © Lippincott Williams & Wilkins. Unauthorized reproduction of this article is prohibited.

Fig. 1

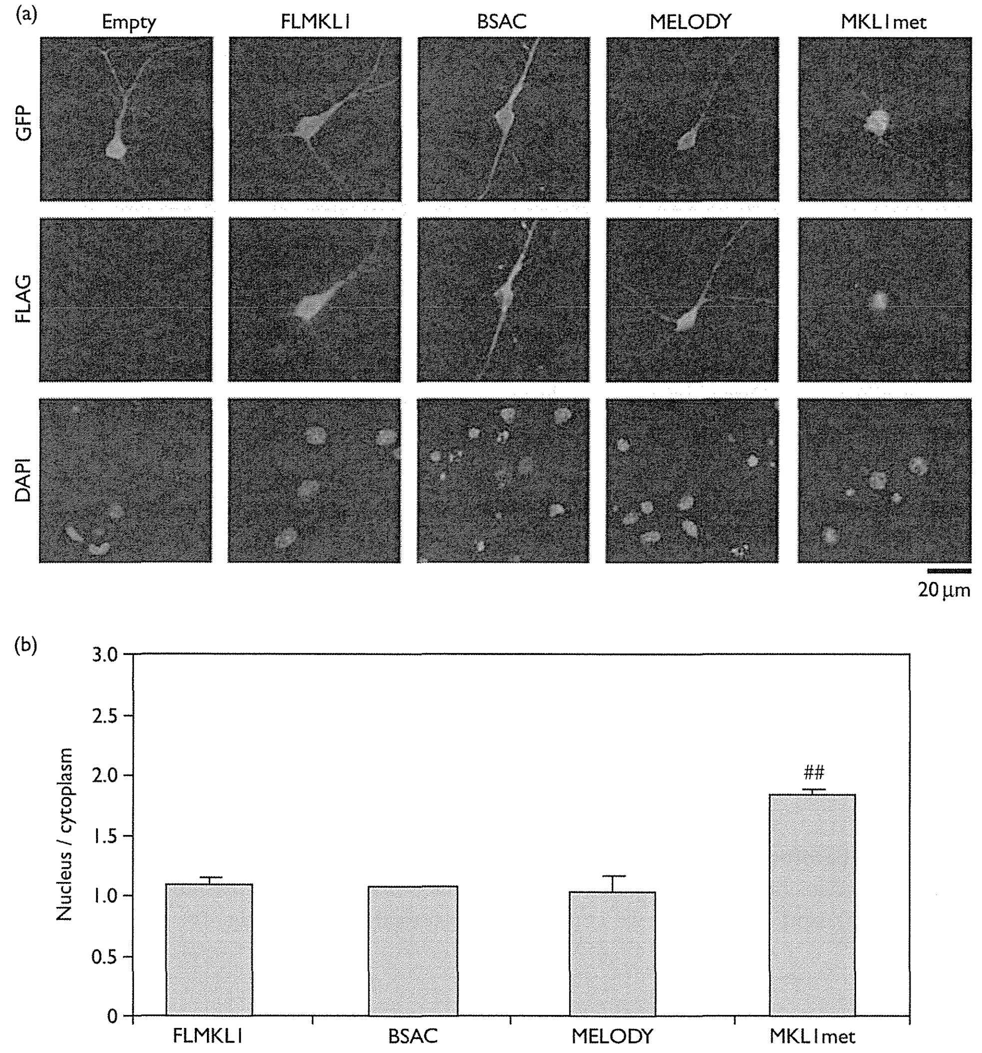

Cellular localization of rat MKL1 isoforms in cortical neurons. (a) Either the empty (empty: 2.0 μg/well), FLAG-tagged FLMKL1 (1.0 μg/well), BSAC (2.0 μg/well), MELODY (1.0 μg/well), or MKL1met (1.5 μg/well) vector was cotransfected with the GFP vector (2.0 μg/well) into rat cortical neurons. To equalize the total amount of vectors (4 μg total/well) used for transfection, the empty vector was added as needed. Cells were fixed 24 h after transfection and stained with anti-GFP antibody (top row), anti-FLAG antibody (middle row), and DAPI (bottom row). Scale bar: 20 μm. (b) The ratio of nuclear/cytoplasmic localization of rat MKL1 isoforms under the experimental conditions shown in (a). Bar graphs represent the mean±SD from three independent experiments ($N=3$). The average value for each experiment was based on evaluation of 20 neurons. The fluorescence intensities of the nucleus and cytoplasm were measured using ZEN software (Zeiss). ##Significance level of $P<0.01$ compared with FLMKL1. BSAC, basic, SAP, and coiled-coil domain; DAPI, 4′,6-diamidino-2-phonylindole; FLMKL1, full-length megakaryoblastic leukemia 1; GFP, green fluorescent protein; MELODY, megakaryoblastic leukemia 1-elongated derivative of yield; MKL1met, megakaryoblastic leukemia 1 met.

in each of three independent experiments used for statistical analyses.

Reporter assay

Transcriptional activity was monitored on the basis of either firefly luciferase or β-galactosidase activity as described previously [14]. In brief, cortical neurons, grown on the six-well plates, were transfected with vectors (4 μg/well) in the following ratios: reporter vector : expression vector = 1 : 3 and firefly luciferase : β-galactosidase = 5 : 1. Cell lysates from cortical neurons were prepared using Tropix lysis solution (Applied Biosystems, Foster City, California, USA). Firefly luciferase and β-galactosidase activities were measured by mixing the cell lysates and substrates. The transcriptional activity was calculated by dividing firefly luciferase activity by β-galactosidase activity.

Morphological analysis

To monitor dendritic morphology of cortical neurons, Sholl analysis was carried out for evaluating dendritic complexity. Detailed procedures have been described

Copyright © Lippincott Williams & Wilkins. Unauthorized reproduction of this article is prohibited.

previously [14]. For measurement of axonal length, a 500-μl cell suspension of cortical neurons (5.0×10^6 cells), freshly prepared from rat embryos, was used for electroporation-mediated transfection using the Amaxa Rat Neuron Nucleofector Kit (Lonza, Allendale, New Jersey, USA). FLAG-tagged MKL1 vectors were cotransfected with the GFP vector into rat cortical neurons by electroporation at 0 DIV. Immediately after transfection, $\sim 4.0 \times 10^5$ cells in DMEM medium containing 10% fetal calf serum with 100 μg/ml kanamycin sulfate were seeded onto the poly-D-lysine-coated 18-mm circular coverslips, onto which 3.0×10^5 cells were already preseeded (total cell number: 7.0×10^5 cells) in 12-well plates. The medium was changed to B27-containing neurobasal medium 3 h after transfection. Forty-eight hours later, cells were fixed and stained with anti-GFP and anti-Tau-1 antibodies and DAPI. ImageJ software (National Institute of Health, Bethesda, Maryland, USA) was used for the measurement of axonal length by tracing Tau-1 and GFP double-positive processes from the cell body.

Statistical analysis

Statistical significance of treatment effects was analyzed by one-way analysis of variance with the Tukey–Kramer post-hoc test. The number of samples is provided in each figure legend.

Results

Nuclear/cytoplasmic localization of rat MKL1 isoforms

To examine possible differences between the localization of FLMKL1, BSAC, MELODY, and MKL1met, we compared the nuclear and cytoplasmic localization of the MKL1 isoforms in rat cortical neurons. FLAG-tagged MKL1 isoforms were cotransfected into cortical neurons with a GFP expression vector, and their nuclear and cytoplasmic localization was quantified (Fig. 1a). As shown in Fig. 1b, the ratio of nuclear/cytoplasmic localization was ~1.0 for FLMKL1, BSAC, and MELODY isoforms, indicating that comparable levels of these three isoforms were localized to the cytoplasm and the nucleus (left three lanes 1–3). In contrast, the ratio of nuclear/cytoplasmic localization of MKL1met was significantly higher than that of the other MKL1 isoforms tested (Fig. 1b; lane 4, $P < 0.01$ compared with FLMKL1). Thus, the nuclear localization of MKL1met was the highest of all four isoforms.

SRF coactivator function of rat MKL1 isoforms

Next, we checked the SRF coactivator function of MKL1 isoforms in cortical neurons (Fig. 2a–c). To detect SRF transcriptional activity, we used the 3DA-Luc reporter vector, which has three SRF binding sites but is devoid of ternary complex factor binding sites [12,17,18], and the SRE reporter vector ($5 \times$ SRE-Luc), which has five SRF binding sites. All four MKL1 isoforms increased SRF-mediated transcriptional responses with MKL1met showing a stronger effect than the other three isoforms in cortical neurons (Fig. 2a and b; $^{*}P < 0.05$ vs. empty; $^{**}P < 0.01$ vs. empty; $^{\#\#}P < 0.01$ vs. FLMKL1). In contrast, all four MKL1 isoforms did not activate cAMP response element-mediated transcription significantly in cortical neurons (Fig. 2c; $P > 0.05$).

Fig. 2

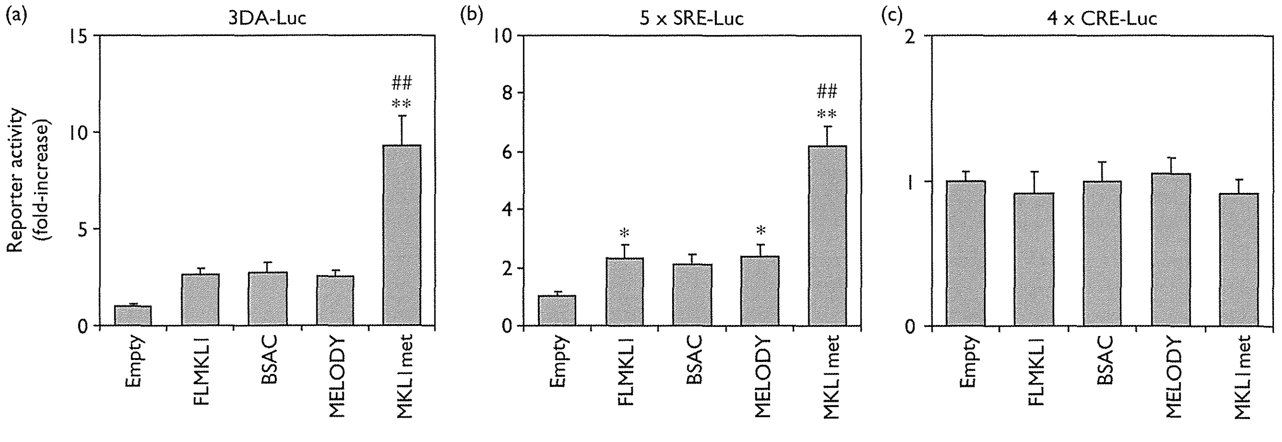

Effects of MKL1 isoforms on SRF-mediated and CREB-mediated transcriptional responses in rat cortical neurons. (a–c) Either the empty (empty: 3.0 μg/well), FLAG-tagged FLMKL1 (1.5 μg/well), BSAC (3.0 μg/well), MELODY (1.5 μg/well), or MKL1met (2.25 μg/well) vector was cotransfected with the firefly luciferase vector indicated [(a) 3DA-Luc, (b) $5 \times$ SRE-Luc, (c) $4 \times$ CRE-Luc, 1.0 μg/well] and the β-galactosidase reporter vector RSV-βgal (0.2 μg/well) into cortical neurons at 7 DIV. Forty-eight hours later, luciferase and β-galactosidase activities were measured. Bar graphs represent the mean±SD [(a) $N=4$; (b) $N=4$; (c) $N=3$] from at least three to four samples. $^{*}P<0.05$ (vs. empty), $^{**}P<0.01$ (vs. empty), $^{\#\#}P<0.01$ (vs. FLMKL1). BSAC, basic, SAP, and coiled-coil domaim; CRE, cAMP response element; CREB, cAMP response element-binding protein; FLMKL1, full-length megakaryoblastic leukemia 1; GFP, green fluorescent protein; MELODY, megakaryoblastic leukemia 1-elongated derivative of yield; MKL1met, megakaryoblastic leukemia 1 met; SRE, serum response element.

Copyright © Lippincott Williams & Wilkins. Unauthorized reproduction of this article is prohibited.

Fig. 3

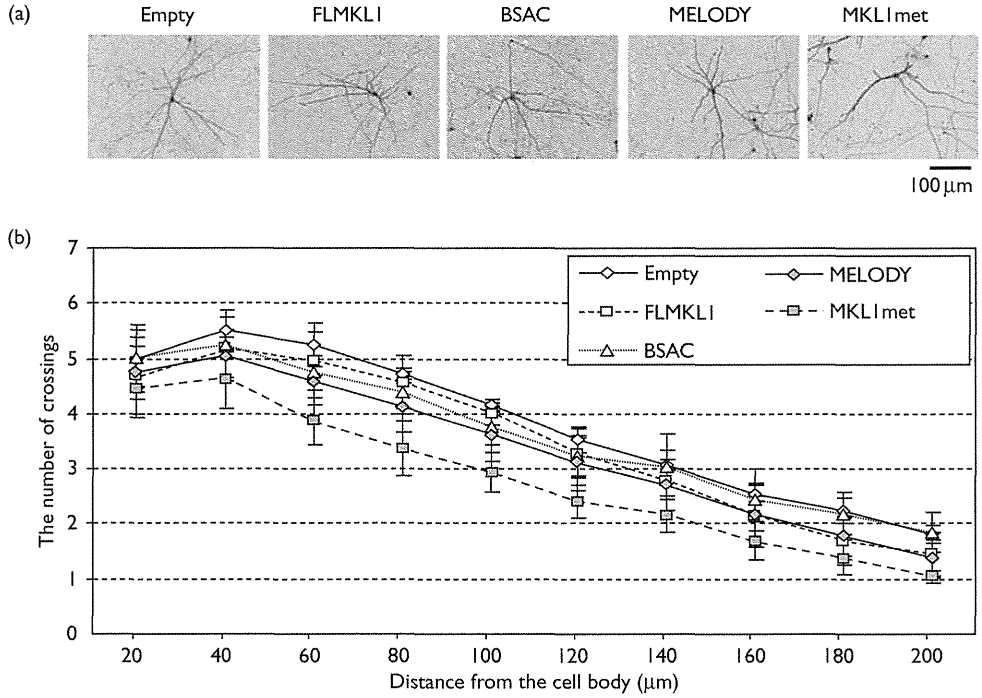

(c)

		Distance from the cell body (μm)									
		20	40	60	80	100	120	140	160	180	200
MKL1FL	vs. Empty	–	–	–	–	–	–	–	–	–	–
BSAC	vs. Empty	–	–	–	–	–	–	–	–	–	–
	vs. FLMKL1	–	–	–	–	–	–	–	–	–	–
Melody	vs. Empty	–	–	–	–	–	–	–	–	–	–
	vs. FLMKL1	–	–	–	–	–	–	–	–	–	–
	vs. BSAC	–	–	–	–	–	–	–	–	–	–
MKL1met	vs. Empty	–	–	**	**	*	*	–	–	–	*
	vs. FLMKL1	–	–	*	*	**	–	–	–	–	–
	vs. BSAC	–	–	–	*	*	–	–	–	–	*
	vs. MELODY	–	–	–	–	–	–	–	–	–	–

Dendritic morphology of cortical neurons expressing rat MKL1 isoforms. (a) Either the empty (Empty: 2.0 μg/well), FLAG-tagged FLMKL1 (1.0 μg/well), BSAC (2.0 μg/well), MELODY (1.0 μg/well), or MKL1met (1.5 μg/well) vector was cotransfected with the GFP vector (2.0 μg/well) into rat cortical neurons at 7 DIV. To adjust the total amount of vectors (4 μg total/well) for transfection, the empty vector was added as needed. Forty-eight hours later, cells were fixed for immunostaining. Images shown were first converted to gray scale and then transformed into negative images. The images were adjusted as follows: brightness −70%. (b) Dendritic complexity analyzed under the experimental conditions shown in (a). Graphs represent the mean±SD from four independent experiments ($N=4$). In each experiment, a minimum of 20 neurons were monitored to obtain the average value. (c) Statistical significance of Sholl analysis in (b). $^{*}P<0.05$, $^{**}P<0.01$. BSAC, basic, SAP, and coiled-coil domain; FLMKL1, full-length megakaryoblastic leukemia 1; GFP, green fluorescent protein; MELODY, megakaryoblastic leukemia 1-elongated derivative of yield; MKL1met, megakaryoblastic leukemia 1 met.

Taken together, these findings suggest that the increased ability of MKL1met to drive SRF-mediated transcription may be because of its higher level of nuclear localization.

Neuronal morphology of cortical neurons expressing rat MKL1 isoforms

Previous studies have shown that MKL1 affects neuronal morphology [14,18]. Accordingly, we examined the effect of rat MKL1 isoforms on the morphology of cortical neurons. Cortical neurons were immunostained after being cotransfected with expression vectors for GFP and one of the FLAG-tagged MKL1 isoforms (Fig. 3). To examine the effect of MKL1 isoforms on dendritic morphology, we carried out Sholl analysis (Fig. 3b). Compared with the control, overexpression of FLMKL1, BSAC, and MELODY had little effect on dendritic number (Fig. 3b; $P>0.05$). In contrast, MKL1met decreased dendritic number (Fig. 3b and c; $^{*}P<0.05$

Copyright © Lippincott Williams & Wilkins. Unauthorized reproduction of this article is prohibited.

Fig. 4

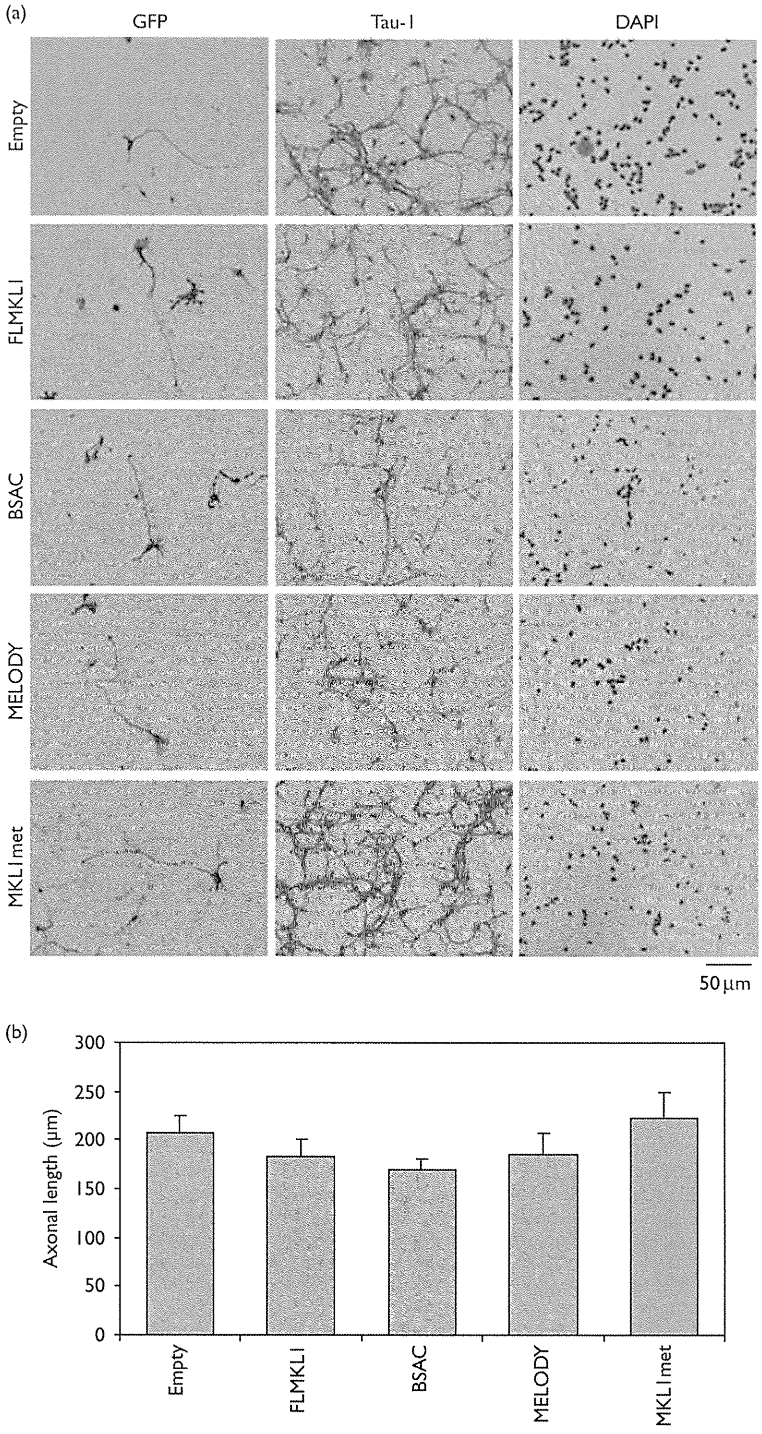

Axonal length of rat cortical neurons expressing MKL1 isoforms. (a) Either the empty (empty: 2.0 µg/well), FLAG-tagged FLMKL1 (1.0 µg/well), BSAC (2.0 µg/well), MELODY (1.0 µg/well), or MKL1met (1.5 µg/well) vector was cotransfected with the GFP vector (2.0 µg/well) into rat cortical neurons using electroporation at 0 DIV. To equalize the total amount of vectors (4 µg total/well) used for transfection, the empty vector was added as needed. Immunostaining and morphological analysis are described in the Materials and methods section. Images shown here were converted to gray scale and then adjusted as follows: brightness −40% and contrast −40%. (b) Axonal length analyzed under the experimental conditions shown in (a). ImageJ software (National Institute of Health) was used for the measurement of axonal length by tracing Tau-1 and GFP double-positive processes from the cell body. Graphs represent the mean±SD from three independent experiments (*N*=3). At least 20 neurons were measured in each experiment. BSAC, basic, SAP, and coiled-coil domain; FLMKL1, full-length megakaryoblastic leukemia 1; GFP, green fluorescent protein; MELODY, megakaryoblastic leukemia 1-elongated derivative of yield; MKL1met, megakaryoblastic leukemia 1 met.

Copyright © Lippincott Williams & Wilkins. Unauthorized reproduction of this article is prohibited.

vs. empty at 100, 120, 200 μm; $*P < 0.05$ vs. FLMKL1 at 60, 80 μm; $*P < 0.05$ vs. BSAC at 80, 100, 200 μm; $*P < 0.01$ vs. empty at 60, 80 μm; $*P < 0.01$ vs. FLMKL1 at 100 μm). We also confirmed that mouse MKL1met exerted similar effects on dendritic number following transfection of rat cortical neurons (data not shown). In contrast, we found that none of the four MKL1 isoforms affected axonal length of cortical neurons significantly (Fig. 4a and b; $P > 0.05$). Taken together, these findings suggest that the most prominent effects of MKL1 isoforms on neuronal morphology are shown by the MKL1met isoform, which selectively affects dendritic morphology.

Discussion

By comparing the localization and function of rat MKL1 isoforms in cultured cortical neurons, we have found that MKL1met differs from the other three isoforms in three ways: increased nuclear localization (Fig. 1), enhanced SRF coactivation (Fig. 2), and reduced dendritic complexity (Fig. 3). As a prominent difference between MKL1 met and the other isoforms is that it contains one less RPEL motif, it is tempting to suggest that the selective effects of MKL1met are due to the reduced number of RPEL motifs. Five G-actin monomers are thought to bind to three RPEL motifs in MKL1 [19]. Therefore, the number of G-actin subunits bound to MKL1met may be lesser than that bound to FLMKL1, BSAC, and MELODY. As free MKL1, released from G-actin, has been shown to be able to translocate into the nucleus in several cell types, it is reasonable to infer that because MKL1met would be bound to fewer G-actin molecules, it may move into the nucleus more readily than the other three MKL1 isoforms in cortical neurons. G-actin also affects the nuclear export and SRF coactivator function of MKL1; interaction of MKL1 with G-actin promotes nuclear export of the complex and G-actin-bound MKL1 is inactive in the nucleus [20]. Thus, the reduced number of RPEL motifs in MKL1met may increase its SRF coactivator function by reducing the suppressive effects of G-actin and increasing its localization in the nucleus. It would be interesting to test in future studies the prediction that deletion of RPEL motifs from BSAC or MELODY would increase nuclear localization and SRF-mediated transcription, as well as decrease dendritic number.

Overexpression of MKL1met reduced the dendritic complexity of cortical neurons (Fig. 3). In contrast, overexpression of MKL2 in cortical neurons increased dendritic complexity [14]. Although overexpression studies indicate that both MKL1met and MKL2 act as SRF coactivators (Ishikawa and colleagues [14,16] and this study), paradoxically, they have opposite effects on dendritic morphology. Taken together, these findings suggest that MKL1- and MKL2- target different genes that play opposite roles in dendritic morphology. However, RNAi-mediated MKL1 and MKL2 knockdown showed the same morphological change, that is, a reduction in dendritic complexity of cortical neurons [14]. Analysis of MKL1/MKL2 double-knockout mice also showed that MKL1 and MKL2 play redundant roles in neuronal migration and neurite outgrowth [15]. To investigate whether MKL1 and MKL2 play differential or redundant roles in brain function, identification of the target genes of MKL1 and/or MKL2 in neurons would likely be helpful.

In summary, we examined the cellular localization and function of rat MKL1 isoforms in neurons and found that MKL1met, which has fewer RPEL motifs than the other three isoforms, shows increased nuclear localization and SRF coactivator function. Further, this isoform reduces dendritic complexity, whereas the other isoforms did not affect this aspect of neuronal morphology. Our previous study reported that rat MKL1 transcripts show differential patterns of expression in the developing and the mature brain [16]. Further studies are warranted to assess whether different MKL1 isoforms influence the expression of different genes. Taken together, these studies suggest that the varying patterns of expression of multiple MKL1 isoforms with distinctive functional properties contribute to the rich heterogeneity in neuronal morphology found in the developing and the adult brain.

Acknowledgements

The authors thank Dr T. Ohtsuka (University of Yamanashi, Japan) for helpful comments on this manuscript.

This study was supported by a grant-in-aid from the Ministry of Education, Culture, Sports, Science, and Technology of Japan (project number: 17790055, 19790052, and 22590080, A.T.; 20390023, M.T.; 23890065, M.I.) and by research grants from the Hayashi Memorial Foundation for Female Natural Scientists (A.T.), Foundation of the first Bank of Toyama (A.T.), Takeda Science Foundation (A.T.), Narishige Neuroscience Research Foundation (A.T.), and the Research Foundation for Pharmaceutical Sciences (A.T.).

Conflicts of interest

There are no conflicts of interest.

References

1 Miano JM. Role of serum response factor in the pathogenesis of disease. *Lab Invest* 2010; **90**:1274–1284.

2 Ramanan N, Shen Y, Sarsfield S, Lemberger T, Schütz G, Linden DG, *et al.* SRF mediates activity-induced gene expression and synaptic plasticity but not neuronal viability. *Nat Neurosci* 2005; **8**:759–767.

3 Etkin A, Alarcon JM, Weisberg SP, Touzani K, Huang YY, Nordheim A, *et al.* A role in learning for SRF: deletion in the adult forebrain disrupts LTD and the formation of an immediate memory of a novel context. *Neuron* 2006; **50**:127–143.

4 Alberti S, Krause SM, Kretz O, Philippar U, Lemberger T, Casanova E, *et al.* Neuronal migration in the murine rostal migratory stream requires serum response factor. *Proc Natl Acad Sci USA* 2005; **102**:6148–6153.

5 Knöll B, Kretz O, Fiedler C, Alberti S, Schütz G, Frotscher M, *et al.* Serum response factor controls neuronal circuit assembly in the hippocampus. *Nat Neurosci* 2006; **9**:195–204.

Copyright © Lippincott Williams & Wilkins. Unauthorized reproduction of this article is prohibited.

6 Buchwalter G, Gross C, Wasylyk B. Ets ternary complex transcription factors. *Gene* 2004; **324**:1–14.

7 Wang DZ, Li S, Hockmeyer D, Sutherland L, Wang Z, Schratt G, *et al.* Potentiation of serum response factor activity by a family of myocardin-related transcription factors. *Proc Natl Acad Sci USA* 2002; **99**:14855–14860.

8 Sasazuki T, Sawada T, Sakon S, Kitamura T, Kishi T, Okazaki T, *et al.* Identification of a novel transcriptional activator, BSAC, by a functional cloning to inhibit tumor necrosis factor-induced cell death. *J Biol Chem* 2002; **277**:28853–28860.

9 Selvaraj A, Prywes R. Megakaryoblastic leukemia-1/2, a transcriptional co-activator of serum response factor, is required for skeletal myogenic differentiation. *J Biol Chem* 2003; **278**:41977–41987.

10 Cen B, Salvaraj A, Prywes R. Myocardin/MKL family of SRF coactivator: key regulators of immediate early and muscle specific gene expression. *J Cell Biochem* 2004; **93**:74–82.

11 Pipes GC, Creemers EE, Olson EN. The myocardin family of transcriptional coactivators: versatile regulators of cell growth, migration and myogenesis. *Genes Dev* 2006; **20**:1545–1556.

12 Miralles F, Posern G, Zaromytidou AI, Treisman R. Actin dynamics control SRF activity by regulation of its coactivator MAL. *Cell* 2003; **113**:329–342.

13 Medjkane S, Perez-Sanchez C, Gaggioli C, Sahai E, Treisman R. Myocardin-related transcription factors and SRF are required for cytoskeletal dynamics and experimental metastasis. *Nat Cell Biol* 2009; **11**:257–268.

14 Ishikawa M, Nishijima N, Shiota J, Sakagami H, Tsuchida K, Mizukoshi M, *et al.* Involvement of the SRF coactivator megakaryoblastic leukemia in the activin-regulated dendritic complexity of rat cortical neurons. *J Biol Chem* 2010; **285**:32734–32743.

15 Mokalled MH, Johnson A, Kim Y, Oh J, Olson EN. Myocardin-related transcription factors regulate the Cdk5/Pctaire 1 kinase cascade to control neurite outgrowth, neuronal migration and brain development. *Development* 2010; **137**:2365–2374.

16 Ishikawa M, Shiota J, Ishibashi Y, Hakamata T, Shoji S, Fukuchi M, *et al.* Identification, expression and characterization of rat isoforms of the SRF coactivator MKL1. *FEBS Open Bio* 2013; **3**:387–393.

17 Tabuchi A, Estevez M, Henderson JA, Marx R, Shiota J, Nakano H, *et al.* Nuclear translocation of the SRF co-activator MAL in cortical neurons: role of RhoA signaling. *J Neurochem* 2005; **94**:169–180.

18 Shiota J, Ishikawa M, Sakagami H, Tsuda M, Baraban JM, Tabuchi A. Developmental expression of the SRF co-activator MAL in brain: role in regulating dendritic morphology. *J Neurochem* 2006; **98**:1778–1788.

19 Mouilleron S, Langer CA, Guettler S, McDonald NQ, Treisman R. Structure of a pentavalent G-actin MRTF-A complex reveals how G-actin controls nucleocytoplasmic shuttling of a transcriptional coactivator. *Sci Signal* 2011; **4**:ra40.

20 Vartiainen MK, Guettler S, Larijani B, Treisman R. Nuclear actin regulates dynamic subcellular localization and activity of the SRF cofactor MAL. *Science* 2007; **316**:1749–1752.

Copyright © Lippincott Williams & Wilkins. Unauthorized reproduction of this article is prohibited.

Stem Cell Reports
Resource

OPEN ACCESS

Long-Term Self-Renewal of Human ES/iPS-Derived Hepatoblast-like Cells on Human Laminin 111-Coated Dishes

Kazuo Takayama,[1,2,3] Yasuhito Nagamoto,[1,2] Natsumi Mimura,[2] Katsuhisa Tashiro,[4] Fuminori Sakurai,[1] Masashi Tachibana,[1] Takao Hayakawa,[5] Kenji Kawabata,[4] and Hiroyuki Mizuguchi[1,2,3,6,*]
[1]Laboratory of Biochemistry and Molecular Biology, Graduate School of Pharmaceutical Sciences, Osaka University, Osaka 565-0871, Japan
[2]Laboratory of Hepatocyte Differentiation, National Institute of Biomedical Innovation, Osaka 567-0085, Japan
[3]iPS Cell-Based Research Project on Hepatic Toxicity and Metabolism, Graduate School of Pharmaceutical Sciences, Osaka University, Osaka 565-0871, Japan
[4]Laboratory of Stem Cell Regulation, National Institute of Biomedical Innovation, Osaka 567-0085, Japan
[5]Pharmaceutical Research and Technology Institute, Kinki University, Osaka 577-8502, Japan
[6]The Center for Advanced Medical Engineering and Informatics, Osaka University, Osaka 565-0871, Japan
*Correspondence: mizuguch@phs.osaka-u.ac.jp
http://dx.doi.org/10.1016/j.stemcr.2013.08.006
This is an open-access article distributed under the terms of the Creative Commons Attribution-NonCommercial-No Derivative Works License, which permits non-commercial use, distribution, and reproduction in any medium, provided the original author and source are credited.

SUMMARY

The establishment of self-renewing hepatoblast-like cells (HBCs) from human pluripotent stem cells (PSCs) would realize a stable supply of hepatocyte-like cells for medical applications. However, the functional characterization of human PSC-derived HBCs was not enough. To purify and expand human PSC-derived HBCs, human PSC-derived HBCs were cultured on dishes coated with various types of human recombinant laminins (LN). Human PSC-derived HBCs attached to human laminin-111 (LN111)-coated dish via integrin alpha 6 and beta 1 and were purified and expanded by culturing on the LN111-coated dish, but not by culturing on dishes coated with other laminin isoforms. By culturing on the LN111-coated dish, human PSC-derived HBCs were maintained for more than 3 months and had the ability to differentiate into both hepatocyte-like cells and cholangiocyte-like cells. These expandable human PSC-derived HBCs would be manageable tools for drug screening, experimental platforms to elucidate mechanisms of hepatoblasts, and cell sources for hepatic regenerative therapy.

INTRODUCTION

Human embryonic stem cells (hESCs) and human induced pluripotent stem cells (hiPSCs) have the ability to self-replicate and to differentiate into all types of body cells including hepatoblasts and hepatocytes. Although cryopreserved primary human hepatocytes are useful in drug screening and liver cell transplantation, they rapidly lose their functions (such as drug metabolism capacity) and hardly proliferate in in vitro culture systems. On the other hand, human hepatic stem cells from fetal and postnatal human liver are able to self-replicate and able to differentiate into hepatocytes (Schmelzer et al., 2007; Zhang et al., 2008). However, the source of human hepatic stem cells is limited, and these cells are not available commercially. Therefore, the human pluripotent stem cell (hPSC)-derived hepatoblast-like cells (HBCs), which have potential to differentiate into the hepatocyte-like cells, would be an attractive cell source to provide abundant hepatocyte-like cells for drug screening and liver cell transplantation.

Because expandable and multipotent hepatoblasts or hepatic stem cells are of value, suitable culture conditions for the maintenance of hepatoblasts or hepatic stem cells obtained from fetal or adult mouse liver were developed (Kamiya et al., 2009; Tanimizu et al., 2004). Soluble factors, such as hepatocyte growth factor (HGF) and epidermal growth factor (EGF), are known to support the proliferation of mouse hepatic stem cells and hepatoblast (Kamiya et al., 2009; Tanimizu et al., 2004). Extracellular matrix (ECM) also affects the maintenance of hepatoblasts or hepatic stem cells. Laminin can maintain the character of mouse hepatoblasts (Dlk1-positive cells) (Tanimizu et al., 2004). However, the methodology for maintaining HBCs differentiated from hPSCs has not been well investigated. Zhao et al. (2009) have reported that hESC-derived hepatoblast-like cells (sorted N-cadherin-positive cells were used) could be maintained on STO feeder cells. Although a culture system using STO feeder cells for the maintenance of hepatoblast-like cells might be useful, there are two problems. The first problem is that N-cadherin is not a specific marker for human hepatoblasts. N-cadherin is also expressed in hESC-derived mesendoderm cells and definitive endoderm (DE) cells (Sumi et al., 2008). The second problem is that residual undifferentiated cells could be maintained on STO feeder cells. Therefore, their culture condition cannot rule out the possibility of the proliferation of residual undifferentiated cells. Because it is known that hPSC-derived cells have the potential to form teratomas in the host, the production of safer hepatocyte-like cells or hepatoblast-like cells has been required. Therefore, we decided to purify hPSC-derived HBCs, which can differentiate into mature hepatocyte-like cells, and then expand these cells.

In this study, we attempt to determine a suitable culture condition for the extensive expansion of HBCs derived